

STRUCTURAL TRANSITION OF
MAGNETORHEOLOGICAL FLUIDS IN MICROGRAVITY

by

Eric Scott Bennung

A thesis submitted to the Faculty of the University of Delaware in partial
fulfillment of the requirements for the degree of Honors Bachelor of Chemical
Engineering with Distinction

Spring 2009

Copyright 2009 Eric S. Bennung

All Rights Reserved

STRUCTURAL TRANSITION OF
MAGNETORHEOLOGICAL FLUIDS IN MICROGRAVITY

by

Eric Scott Bennung

Approved: _____
Eric M. Furst, Ph.D.
Professor in charge of the thesis on behalf of the Advisory Committee

Approved: _____
Antony N. Beris, Ph.D.
Committee member from the Department of Chemical Engineering

Approved: _____
Norbert Mulder, Ph.D.
Committee member from the Board of Senior Thesis Readers

Approved: _____
Alan Fox, Ph.D.
Director, University Honors Program

Acknowledgements

I would like to acknowledge and thank certain people and organization for their support.

Dr. Eric Furst, the Principle Investigator of the InSPACE experiments, offered me the chance to get involved with undergraduate research. He opened the door for me to become a part of the process and analysis of very cutting edge science, and I thank him for that and his guidance throughout my research experience.

Dr. Paula Vasquez, a postdoctoral researcher from the Furst Group, also assisted in guiding me in undergraduate research. Her help and support was invaluable while I conducted my research.

The entire Furst Group was helpful through the research process.

The University of Delaware and the Undergraduate Research Program have both given me great opportunity during my four years of college.

Dr. Alice Gast, the previous PI of the InSPACE experiments, and her team of researchers provided valuable resources for my research.

The institution of NASA funded my research, and I am indebted to members of the NASA team. My research could not have been completed without the help of Juan Agui, Researcher from NASA Glen Research Center, as well as the International Space Station Officers Peggy Whitson, Donald R. Pettit, William McArthur, and Jeff Williams.

Lastly, I would like to thank my family. They mean everything in the world to me. Without their love and support, I would never have reached the level of academic and life experience that I have achieved thus far.

Contents

List of Figures	vi
List of Tables	viii
Nomenclature	ix
Abstract	x
1 Introduction	1
1.1 Magnetorheological Fluids	1
1.1.1 Parameters & Properties	1
1.1.2 Practical Applications	5
1.2 Motivation	6
1.2.1 Microgravity	7
1.2.2 Theoretical and Broader Impact	8
1.2.3 Summary	9
2 Experimental Methods	11
2.1 InSPACE	11
2.1.1 InSPACE 1	11
2.1.2 InSPACE 2	12
2.2 Helmholtz Coil	14
2.3 Microgravity Science Glovebox	15
3 Image Processing	17
3.1 Pre-processing	18
3.2 Intensity Differences	18
3.2.1 Histogram Specification	19
3.2.2 High/Low Pass Filter	20
3.3 Local Histogram Equalization	23
3.4 Binary Image	24

4	Data Collection	25
4.1	Statistical Analysis	25
4.2	Number Density & Average Aggregate Size	25
4.3	Average Inter-Aggregate Spacing	26
5	Kinetics of Aggregation	27
5.1	Observations	27
5.2	The Smoluchowski Equation	28
5.3	Number Density of Aggregates	30
	5.3.1 InSPACE 1	31
	5.3.2 InSPACE 2	32
5.4	Inter-aggregate Spacing	36
	5.4.1 InSPACE 1	37
	5.4.2 InSPACE 2	38
5.5	Aggregate Cross-sectional Area	40
	5.5.1 InSPACE 1	43
	5.5.2 InSPACE 2	44
5.6	Discussion	46
	5.6.1 Values of z comparison	46
	5.6.2 Dynamic Scaling Theory	49
6	Time Scaling of Kinetic Results	52
6.1	Time Scaling	52
6.2	InSPACE 1	55
6.3	InSPACE 2	58
6.4	Nucleation Step of Aggregation	60
7	Conclusions	61
	Bibliography	64
A	InSPACE Data Catalog	67
A.1	InSPACE 1 - ST View	68
A.2	InSPACE 1 - RT view	80

List of Figures

1.1	Dipole particle interaction	2
1.2	MR fluid transition to chains	3
1.3	MR fluid aggregation method diagram	4
1.4	The Dong Ting Lake Bridge in China	5
1.5	MR damped washing machine	6
1.6	Proposed MR fluid controlled NASA robot	7
1.7	Catastrophic sedimentation of a suspension in a gravitational field	8
2.1	Helmholtz Coil	15
2.2	Microgravity Science Glovebox Experimental Setup	15
3.1	Gray-Scale Processing	18
3.2	Histogram Equalization Process	20
3.3	High/Low Pass Image Sequence	22
3.4	Local Histogram Processing	23
3.5	Binary Image Results	24
4.1	Histogram of Aggregate Size	26
4.2	Delaunay Triangulation	26
5.1	Number Density of Aggregates vs. Time - InSPACE 1	32
5.2	Number Density of Aggregates vs. Time - InSPACE 1	34
5.3	Visual representation of cell depth comparison	35
5.4	Plane of view comparison	36
5.5	Average Inter-aggregate Spacing vs. Time - InSPACE 1	38
5.6	Average Inter-aggregate Spacing vs. Time - InSPACE 2	39
5.7	Hexagonal Cross Sectional Particle Structure with Circular Radius Representation	40
5.8	Radius of Cross Section as Function of Number of Particles	42
5.9	Exaggerated depiction of possible oblique cross-sectional measurements	43
5.10	Average Cross-sectional Area vs. Time - InSPACE 1	43
5.11	Average Cross-sectional Area vs. Time - InSPACE 2	45
5.12	z vs. characteristic length ratio - InSPACE 1	48
5.13	z vs. characteristic length ratio - InSPACE 2	48
6.1	r_c as a function of θ	54

6.2	Number Density of Aggregates vs. t/t^* - InSPACE 1	56
6.3	Average Inter-aggregate Spacing vs. t/t^* - InSPACE 1	56
6.4	Average Cross-sectional Area vs. t/t^* - InSPACE 1	57
6.5	Number Density of Aggregates vs. t/t^* - InSPACE 2	58
6.6	Average Inter-aggregate Spacing vs. t/t^* - InSPACE 2	59
6.7	Average Cross-sectional Area vs. t/t^* - InSPACE 2	59
6.8	Representation of proposed activation barrier to aggregation	60

List of Tables

2.1	InSPACE 1 λ values for various parameters	13
2.2	InSPACE 2 Volume Fractions	13
2.3	InSPACE 2 Field strengths and λ values	14
5.1	Values of z from Number Density - InSPACE 1	32
5.2	Values of z from Number Density - InSPACE 2	35
5.3	Values of z from Inter-aggregate Spacing - InSPACE 1	38
5.4	Values of z from Inter-aggregate Spacing - InSPACE 2	39
5.5	Power-law Dependence of Average Cross-sectional Area - InSPACE 1	44
5.6	Power-Law Dependence of Average Cross-sectional Area - InSPACE 2	45
5.7	z Comparison - InSPACE 1	47
5.8	z Comparison - InSPACE 2	47

Nomenclature

a	particle radius	μm
H	field strength	A/m
r	particle separation	μm
U	dipole particle interaction	J
T	temperature	K
k_B	Boltzmann constant	J/K
t	time	s
N	number of aggregates	-
$\langle R \rangle$	average inter-aggregate separation	μm
$\langle A \rangle$	average aggregate cross sectional area	μm^2
s_k	number of chains with length k	-
$\langle s \rangle$	average number particles in a chain	-
D	diffusion coefficient	$\mu\text{m}^2/\text{s}$
z	Smoluchowski exponent	-
t_B	doublet time	s
K_{ij}	reaction kernel of Smoluchowski equation	
λ	dimensionless field strength	-
ϕ	volume fraction	-
θ	angle of separation between r and H	-
γ	diffusion exponent	-

Abstract

Magnetorheological (MR) fluids exhibit unique mechanical and rheological properties when subjected to a magnetic field. MR fluids greatly increase their viscosity through rapid formation of chains of dipoles along the direction of the field. Lateral cross-linking of these chains allows the fluid support stress perpendicular to the applied field. Thus, MR fluids undergo a large, fast, and reversible transition from a liquid-like to a solid-like state upon the application of a magnetic field. This provides an excellent basis for a vast number of applications, such as actively controlled dampers and actuators.

This thesis presents observations and analysis of experiments performed as part of the InSPACE NASA program. The experiments were performed on the International Space Station (ISS). The InSPACE goal is to understand the long-time three-dimensional aggregation kinetics of MR fluids under steady and pulsed magnetic fields by testing models and hypotheses. This thesis focuses on this evolution of MR aggregates. Studies such as these are complicated on Earth due to the rapid sedimentation induced by gravity. Video microscopy experiments were performed in the ISS microgravity science glovebox. Aggregation kinetics were studied as a function of field- and sample-based parameters. Images gathered from the videos were prepared for data collection with proper image processing parameters. Particle tracking algorithms were then applied to extract quantitative data. Specific data on the kinetics of aggregation comes in the form of the time evolution of the number density of aggregates, the inter-aggregate separation, and the average aggregate size. The data analysis is based on the Smoluchowski equation.

Chapter 1

INTRODUCTION

1.1 Magnetorheological Fluids

Magnetorheological (MR) fluids are colloidal suspensions that exhibit unique properties when subjected to a magnetic field. Most importantly, the rheology of MR fluids changes rapidly to a solid-like state due to the formation of chains of paramagnetic particles along the direction of the field. Lateral cross-linking of these chains allows the fluid to support stress perpendicular to the applied field, giving rise to the rheological yield stress and solid-like behavior. Ultimately, this leads to a large, fast, and reversible transition from a liquid-like to a solid-like state.[\[1, 2\]](#)

1.1.1 Parameters & Properties

The non-dimensional field strength, λ , is one of the key parameters that determines the state of an MR fluid. As defined in Equation [1.1](#), a magnetic field strength, H , will induce magnetic moments, μ , in the colloidal particles with radius

a and magnetic susceptibility, χ . [1, 3]

$$\mu = \frac{4}{3}a^3\mu_o\chi H \quad (1.1)$$

The dipole interaction energy between two particles is a function of the radius of separation of the particles, r , and the angle that they form relative to the magnetic field, θ . It is defined in Equation 1.2. The relationship between r and θ to the direction of the magnetic field and location of particles is depicted in Figure 1.1.[1]

$$U(r, \theta) = \frac{\mu^2}{4\pi\mu_o} \frac{1 - 3\cos^2(\theta)}{r^3} \quad (1.2)$$

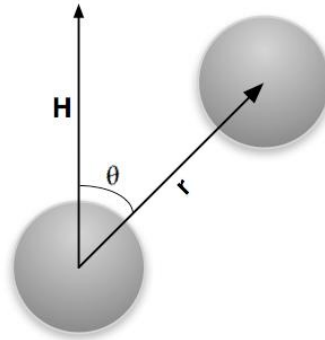


FIGURE 1.1: Dipole particle interaction

The dipole interaction potential reaches a maximum when $r = 2a$, the diameter of a particle, and $\theta = 0$, meaning the particles are touching and are in line with the magnetic field. Equation 1.3 defines the non-dimensional field strength, λ , as the ratio between this maximum dipole interaction potential and the thermal energy of

the system, defined as the Boltzmann constant, k_B , multiplied by the temperature, T . When the dipole interaction is much greater than the thermal energy, $\lambda \geq 1$, and the particles begin to interact with each other due to their magnetic dipole. This marks the beginning of the transition from dispersed particles to aggregated chains of particles; however, λ must be much larger to form chains.[1]

$$\lambda = \frac{-U_{max}}{k_B T} = \frac{\pi \mu_o \alpha^3 \chi^2 H^2}{9 k_B T} \quad (1.3)$$

A depiction of this transition is shown in Figure 1.2, where H is the applied magnetic field with direction indicated by the arrow.

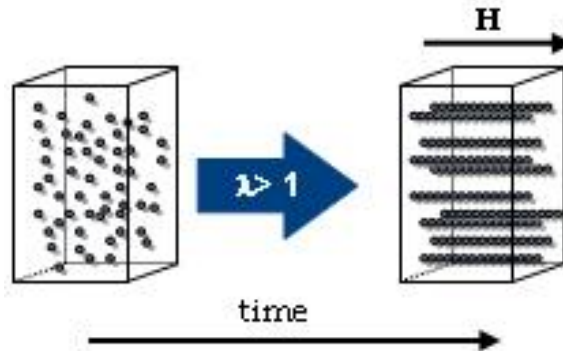


FIGURE 1.2: MR fluid transition to chains

In addition to the field strength, the volume fraction of the dispersed phase (the paramagnetic particles), ϕ , plays a significant role in the final structure of the fluid. Figure 1.3, a phase diagram developed by Furst and Gast, demonstrates the effects of λ and ϕ on how the chains are expected to aggregate.[4] The kinetic pathway by which the chains aggregate in turn dictates the final structure of the

fluid. λ influences the stiffness of chains and the potential for trapping of chain defects, while ϕ influences the distance over which interaction occurs. Dipolar chains formed in suspensions with low ϕ interact over long distances, while systems with high ϕ interact in close proximity.[4, 5]

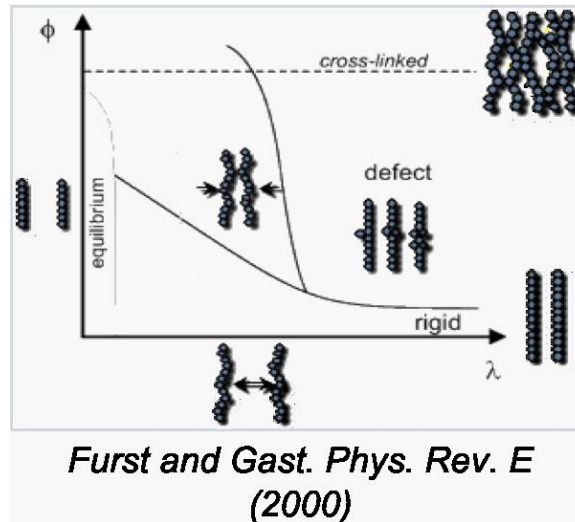


FIGURE 1.3: MR fluid aggregation method diagram

As will be discussed in further detail in chapters 5 and 6, the kinetics of aggregation are diffusion limited until the particles diffuse within capture radius dictated by the strength and range of the dipolar interactions. At this point, the particles exhibit ballistic motion and aggregate immediately.[3, 6] The capture radius is a function of λ , and since the effective size of the particles is increased by this capture radius, ϕ is effectively increased. Based on this and the other aspects of the fluid that these parameters control, it is evident that they both have significant effects on the kinetics of aggregation.[3, 4] There are distinct phase regions within this diagram that correspond to specific methods of growth. One of particular

interest is the critical cross-linking volume fraction. Above this volume fraction, the transition to solid-like behavior is possible if λ is strong enough.[4]

1.1.2 Practical Applications

Because of their interesting and unique properties, the applications for MR fluid are diverse. The most extensive applications for MR fluids are in actively controlled dampers and actuators.[1, 7] For instance, seismic dampers with MR fluids operate at the building resonance frequency and absorb the destructive shock waves and oscillations from earthquakes and weather events, reducing or eliminating structural damage. The Dong Ting Lake Bridge in China, shown in Figure 1.4, uses MR fluid dampers to counter gusts of wind.[7]



FIGURE 1.4: The Dong Ting Lake Bridge in China

MR fluid dampers have made their way into everyday machinery, such as automobiles and washing machines, in order to improve shock-absorption.[8] The washing machine represents an interesting example of a standard machine that requires compromise between vibrational control and optimum system performance.

As opposed to normal shock absorbing systems, a variable damping system based on MR fluids can help mitigate this compromise. As shown in Figure 1.5, by actively controlling the damping of the system, the vibration control of the system can be optimized. This is done by increasing the damping as the machine passes through resonance and off again at the highest speeds. This takes advantage of the benefits of both high and low damping systems and eliminates the violent shaking that leads to early breakdown.[8]

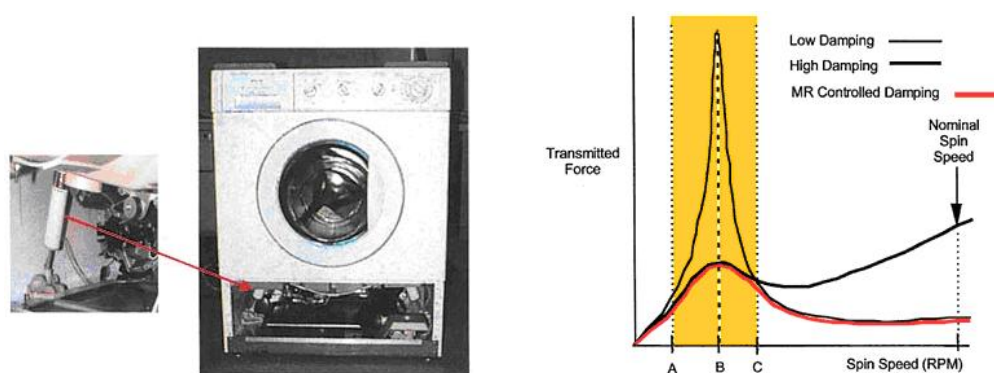


FIGURE 1.5: MR damped washing machine

MR fluids are envisioned for numerous space exploration purposes. These include improvement in equipment such as robots, plant rovers, and crew suits through enhancement in fatigue countermeasure and mechanical sensors.[7]

1.2 Motivation

This thesis is part of a larger collaboration between the University of Delaware and NASA, "Investigating the Structure of Paramagnetic Aggregates from Colloidal Emulsions" (InSPACE). The project's principal investigator is Dr. Eric



FIGURE 1.6: Proposed MR fluid controlled NASA robot

Furst, and I, in close collaboration with his postdoctoral researcher, Dr. Paula Vasquez, are analyzing the results of the InSPACE experiments, which are performed in the Microgravity Science Glovebox (MSG) facility onboard the International Space Station (ISS). These experiments investigate how the effects of the field-strength and sample-based variables affect the structural evolution of the fluid. The focus of this thesis is on the kinetics of structure formation in DC fields. Previous works have studied similar experiments with similar objectives [3, 6, 9], but what sets these experiments apart is their ability to investigate very long time behavior.

1.2.1 Microgravity

The reason these studies are performed in microgravity stem from the complications on Earth due to rapid gravitational sedimentation. The InSPACE experiments study volume fractions much less than the critical value needed to form a

percolated structure. Therefore, the structure is not fully interconnected. Since the typical density of the particles used to create these fluids is 1.5 times greater than that of the carrier fluid, the structure, consisting of dispersed dipolar chains sediments, as illustrated in Figure 1.7, where all the particles have sedimented to the bottom of the sample. Microgravity allows for an in detail study of the aggregation kinetics of MR structures, even at very long times.[10]

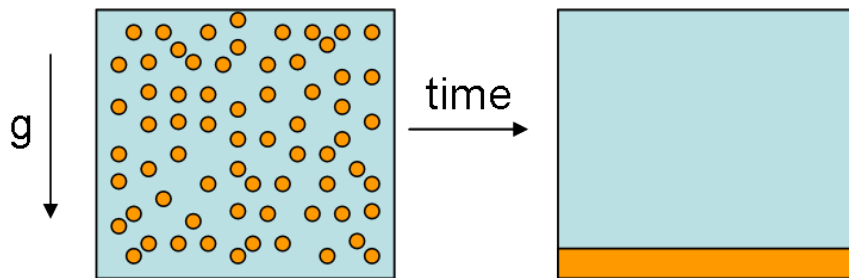


FIGURE 1.7: Catastrophic sedimentation of a suspension in a gravitational field

1.2.2 Theoretical and Broader Impact

Many aspects of this project make it of interest for both its intellectual merit as well as its broader applications. A long-standing aim of complex fluid rheology by identifying the fundamental roles that interactions on small length scales play in determining the rheological properties of materials. MR fluids provide a great example of these critical interactions. [5, 11] The broader impact of this work is in providing a basis for new technologies both on Earth and in space. As stated in the previous section, current technologies based on MR fluids include tunable dampers and brakes, while future application in robotics, clutches, and

other vibration-control systems, such as seismic damping of structures, are envisioned. Understanding how these fluids work at the fundamental level will better enable us to improve upon the use of MR fluids in these fields and to expand MR fluids use in other applications as well.

1.2.3 Summary

- Chapter 1 - Introduction

In this chapter, background about MR fluids, including properties and parameters as well as practical applications, is discussed. The motivations of the thesis are outlined as the study of the long time aggregation kinetics of MR fluids

- Chapter 2 - Experimental Methods

In this chapter, the details of the experimental procedure are discussed. The parameters of each experiment are noted.

- Chapter 3 - Image Processing

The image processing techniques used to clean the raw video microscopy is discussed in detail. The image is pre-processed and intensity differences are mitigated. The image is then passed through a series of filters and other image processing procedures to remove noise and enhance contrast.

- Chapter 4 - Data Collection

Data about the number density, inter-aggregate spacing, and average cross-sectional area is extracted from each processed image. The details of the collection including statistics are discussed

- Chapter 5 - Kinetics of Aggregation

The data of number density, inter-aggregate spacing, and average cross-sectional area are plotted and analyzed against time. The data is analyzed under through the Smoluchowski equation for irreversible colloidal aggregation.

- Chapter 6 - Time-Scaling

The kinetic data from chapter 5 is scaled by a time constant such that the data is plotted against non-dimensional time. The time constant is a function of both ϕ and λ , allowing experiments with varying parameters to be compared more readily.

- Chapter 7 - Conclusion

Conclusions from the thesis are presented.

Chapter 2

EXPERIMENTAL METHODS

2.1 InSPACE

InSPACE has been separated into two increments. InSPACE 1 was conducted in 2003 and 2006, while InSPACE 2 occurred in 2008. InSPACE experiments were performed in the MSG facility onboard ISS by NASA Officers Peggy Whitson, Donald R. Pettit, William McArthur, and Jeff Williams. In this thesis, we focus on the analysis of experiments under the application of DC magnetic fields. Analysis of the microscopic structures of the fluids will provide a better understanding of the long-time aggregation kinetics of MR fluids in DC fields.

2.1.1 InSPACE 1

InSPACE 1 experiments were conducted on the ISS in two separate phases; the first of which was performed during 2003, and the second phase was done in 2006.

The samples prepared for InSPACE 1 were ferrofluid emulsions consisting of iron oxide particles, Isopar M (an isoparaffinic hydrocarbon solvent), and surfactant suspended in a solution of sodium dodecyl sulfate (SDS), an anionic surfactant, and ultra-pure water. These samples were comprised of particles of uniform size, but size was varied across different experiments. Diameters of the particles were 0.31, 0.40 and 0.66 μm . These particles had a magnetic susceptibility, $\chi = 1.5$. Magnetic susceptibility is the degree of magnetization a material experiences in response to an applied magnetic field. The volume fraction of the particles was kept at a constant 0.2%. The field-based parameters of field strength and pulse frequency were also varied. During InSPACE 1 the field strength spanned a large range, from 600 to 2082 A/m.

As previously noted in Equation 1.3, the non-dimensional field strength, which determines the structural state of the suspension or emulsion, λ is a function of both the field strength and the particle size. Table 2.1 contains the values of λ based on both of the parameters. The bold values indicate experiments in which a DC field was applied and are analyzed in this study.

2.1.2 InSPACE 2

The InSPACE 2 experiments were conducted in 2008. The samples prepared for InSPACE 2 were suspensions of paramagnetic particles rather than the ferrofluid

TABLE 2.1: InSPACE 1 λ values for various parameters

Field Strength [A/m]	Particle Diameter, $2a$ [μm]		
	0.31	0.40	0.66
2082	3.87	8.32	37.4
2021	3.65	7.84	35.2
1997	3.56	7.66	34.4
1816	2.95	6.33	28.4
1513	2.05	4.40	19.7
600	0.32	0.69	3.10

emulsions used for InSPACE 1; however, the carrier fluid in the samples was similar. For InSPACE 2, NaN_3 was used in small concentrations as a bactericide. The paramagnetic particles used in these experiments were super-paramagnetic latex particles (Dynabeads, Invitrogen), which are made of highly cross-linked polystyrene nanoparticles with an even dispersion of magnetic material throughout the particles in the form of γ - Fe_2O_3 and Fe_3O_4 . The particle size in these experiments was kept constant at 1.05 micrometers, and the magnetic susceptibility, $\chi = 1.4$. The volume fraction of the particles in the system was varied from 0.40% to 0.65%. A complete list of the volume fractions is found in Table 2.2. The bold values indicate experiments in which a DC field was applied and are analyzed in this study.

TABLE 2.2: InSPACE 2 Volume Fractions

Volume Fraction [-]
0.0040
0.0048
0.0056
0.0065

The field strength was also varied during InSPACE 2, from $H = 1000$ to 2000 A/m in increments of 500 A/m. This corresponds to given values of λ indicated in Table 2.3.

TABLE 2.3: InSPACE 2 Field strengths and λ values

Field Strength [A/m]	λ [-]
2000	120.9
1500	68.00
1000	30.22

2.2 Helmholtz Coil

The magnetic fields for these experiments were generated using a Helmholtz coil. A Helmholtz coil produces a region of nearly uniform magnetic field using two identical circular magnetic coils. The coils must be spaced apart by a distance equal to the radius of the coils in order for the coil to generate a uniform field. Each coil carries an equal electrical current in the same direction and the generated field is perpendicular to the coils. The magnitude of the field generated is varied simply by varying the current, I , as shown in Equation 2.1. This relationship is derived from the Biot-Savart law. Figure 2.1 depicts a Helmholtz coil, with the important qualities denoted, and the coil used in the InSPACE experiments.

$$H = \left(\frac{4}{3}\right)^{\frac{3}{2}} \left(\frac{\mu_o N I}{R}\right) \quad (2.1)$$

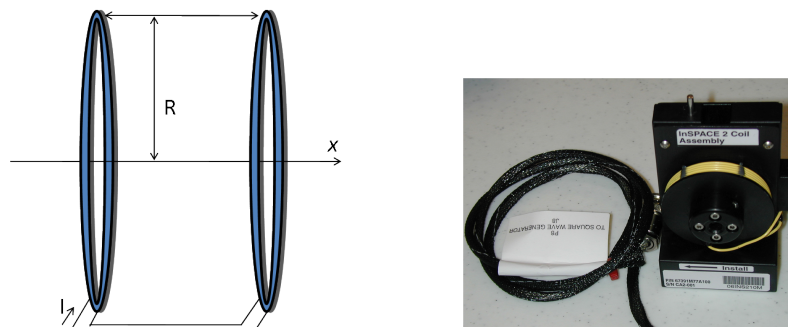


FIGURE 2.1: Helmholtz Coil

2.3 Microgravity Science Glovebox

The experimental setup within the MSG is shown in Figure 2.2. The experimental cell and Helmholtz coil was adhered to the MSG. Next, the crew member running the experiment installed the optics assembly that includes two cameras for imaging and a backlighting system illuminating the samples.

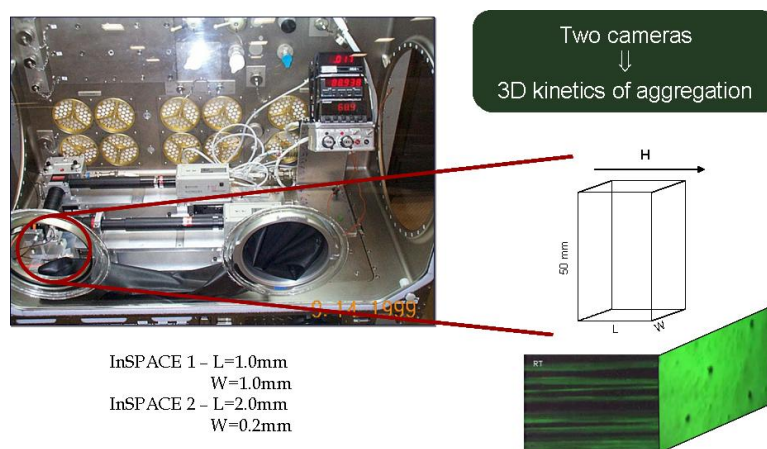


FIGURE 2.2: Microgravity Science Glovebox Experimental Setup

With the implementation of two cameras, this setup allows for the study of three-dimensional aggregation kinetics. As displayed in Figure 2.2, the two camera angles provide views parallel and perpendicular to the magnetic field. This thesis

focuses on the steady field aggregation kinetics in the perpendicular view, also called straight-on view (ST). The parallel camera view is called right angle view (RT). The dimensions of these two camera angles are noted below.

ST: 0.350 mm x 0.260 mm

RT: 0.360 mm x 0.260 mm

Besides different sample and field parameters, one of the other key differences between the InSPACE 1 and 2 experiments included the size of the cell and the camera views. InSPACE 1 used a cell size of 1.0 x 1.0 x 50 mm while InSPACE 2 used a cell size of 2.0 x 0.2 x 50 mm. This possibly allows for the investigation on the effects of confinement.

Finally, the video microscopy experiments were run with the varying parameters. A current corresponding to these parameters was flowed to the coil to produce a uniform DC magnetic field. This field caused the particles to interact and aggregate to form microstructures within the fluid. The cameras record this aggregation process as videos. These videos were collected on mini DV cassettes and returned to earth. During the InSPACE 2 experiments, video was also collected via direct downlink from the ISS. Once collected, the data was cataloged and organized. This was of extreme importance. An appendix of the cataloged data from InSPACE 1 is attached.

Chapter 3

IMAGE PROCESSING

In order to gather quantitative data from the InSPACE experiments, the raw video microscopy data was cleaned and filtered. Initial work performed by Dr. Paula Vasquez on the InSPACE 1 videos identified optimal image processing methods to extract quantitative structural information from the ISS video microscopy data. I then used a similar image processing procedure on the InSPACE 2 data. This is a very manual procedure, however, some automation can be achieved through computer programming. The image is pre-processed and intensity differences are removed. The image is then passed through a series of filters and other image processing procedures to remove noise and enhance contrast.

Individual frames were extracted from the videos. The corresponding times at which these frames were taken were recorded so that later the kinetics of aggregation can be analyzed.

3.1 Pre-processing

The pre-processing consists of the removal of the time stamp and conversion from a color image to a gray-scale image. This facilitates the next steps in image processing as well as the final analysis of the image. The results from this process are shown in Figure 3.1.

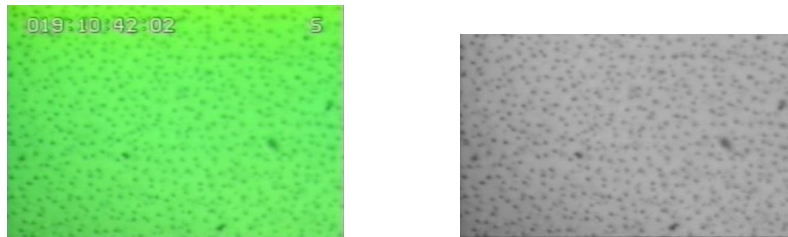


FIGURE 3.1: Gray-Scale Processing

3.2 Intensity Differences

One of the main difficulties with analyzing the kinetics of aggregation is intensity differences in the images. The images were taken either from cassettes transported back to earth or from a direct downlink from the ISS. Depending upon the strength of signal of the downlink, the focusing of the microscopy camera, and the backlighting of the image, the overall intensity of the image changes. There are intensity differences within an individual image and across several images. If ignored, these changes in intensity drastically affect the end result of the image processing, and distorts the results obtained. The next two sections detail the methods used to mitigate the intensity changes.

3.2.1 Histogram Specification

The first process that was applied was a histogram specification. The this process has been shown to eliminate intensity differences between images by matching the histogram of the output image to a specified histogram.[12]

An image with a broad intensity spectrum was chosen as a base case for the specified histogram. The reference image and its histogram are shown in Figure 3.2(a) and (b). Figure 3.2(c) and (d) show the input image and its histogram. Figure 3.2(c) and (d) show equalized image and its histogram.

This process was performed in MATLAB by matching the histogram of the input image as closely as possible to the histogram of the reference image. This is done by shifting the intensity peaks in the input image to difference values on the gray scale, such that equalized histogram resembles the reference histogram. This results in an increase in the contrast of the input image and a decrease in the intensity difference between the input and the reference image. The same decrease in intensity difference would be true for an input image that had a broader histogram than the reference image, except that the contrast would be decreased. The same reference image was used for all image processing. As shown by the images in Figure 3.2, this process is fairly effective in removing this type of intensity difference.

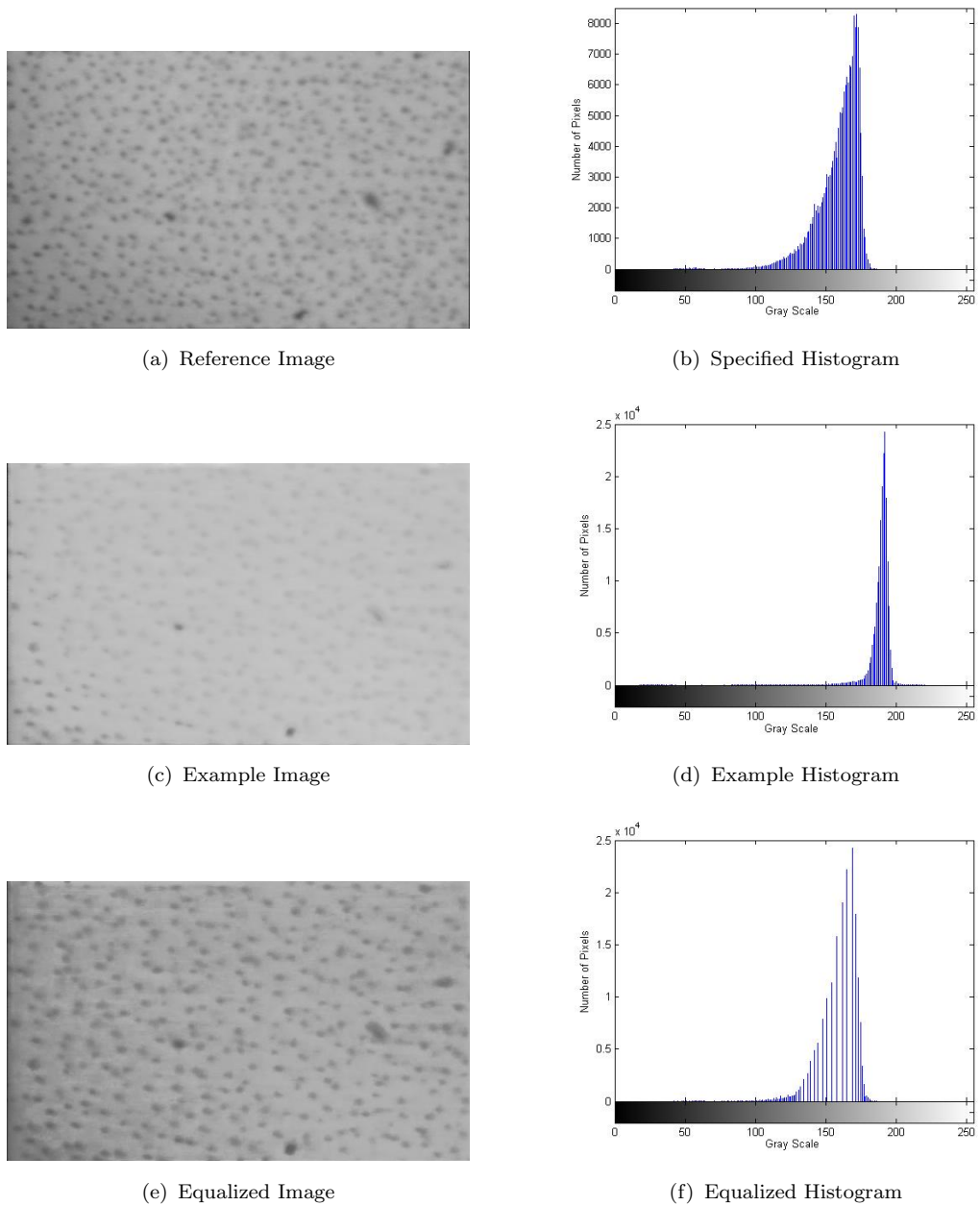


FIGURE 3.2: Histogram Equalization Processing

3.2.2 High/Low Pass Filter

In order to remove spatial variations of intensity within individual images, a high/low pass filter was applied. Low-pass filters attenuate image components

with a high spatial frequencies and remove neighboring pixel-pixel noise. This results in a smoothing effect.[12] Conversely, high-pass filters attenuate the low spatial frequencies image. This results in a flattening effect.[12] High-pass filters are often used in conjunction with low-pass filters. The image can be smoothed with a low-pass filter, and then a high-pass filter can be applied to preserve the aggregate boundary detail.[12]

The following sequence of images shows the high/low-pass filter technique that is applied using the ImageJ software suite. Figure 3.3(a) is the equalized histogram image from the previous process. A rolling ball algorithm with a size of 50 pixels is used to subtract the background to get to Figure 3.3(b). This size of the rolling ball was determined by the average size of the aggregates. It is set large enough to allow the aggregates to get through the filter, but small enough to still subtract the background. The same size rolling ball was used on all experiments.

This image is then converted into Fourier space via a Fast Fourier Transform where the high and low pass filters are applied, shown in Figure 3.3(c). The low pass filter is applied outside the outer circle, removing the low spatial frequencies. The high pass filter is difficult to distinguish, but it removes out the highest spatial frequencies at the center of the image.[12] A smaller low-pass filter led to an image that was too smoothed and thus too blurry to extract meaning full information. A larger high-pass filter led to an image that was too sharpened and thus too dark.

The inverse Fourier transform is taken of the filtered image, as shown in Figure 3.3(d), and the same subtracting background technique is applied to get to Figure 3.3(e). This final figure is exported to Matlab for further processing.

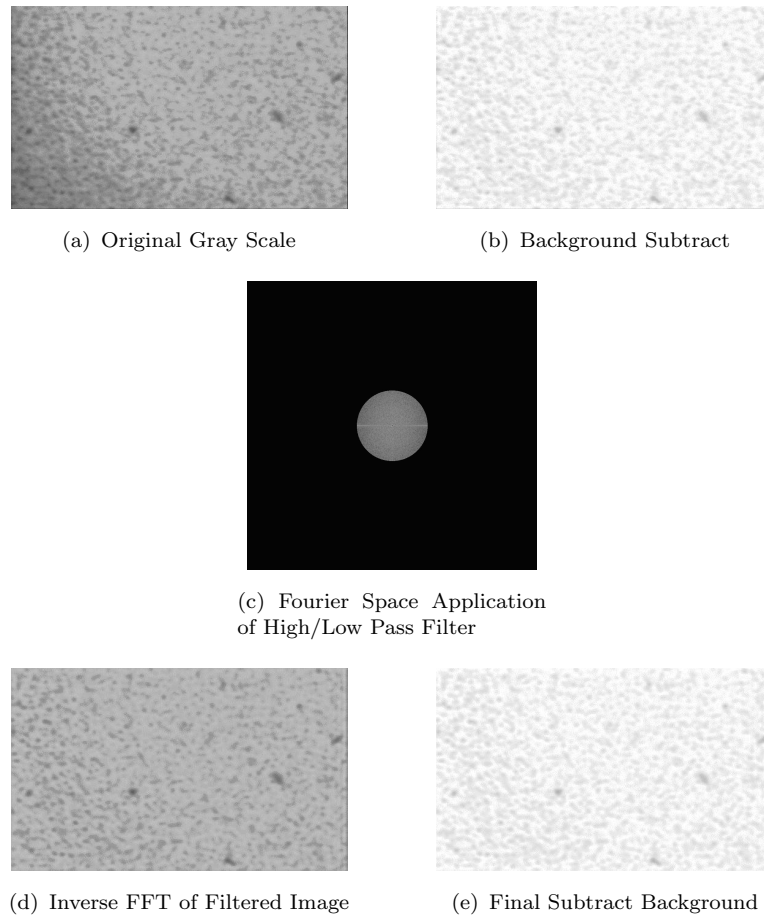


FIGURE 3.3: High/Low Pass Image Sequence

As seen in the sequences of images in Figure 3.3, the high/low-filter combination was able to remove intensity differences within this image relatively well. This is best illustrated by comparison between Figure 3.3(a) and (d). In the original

image, the left side of the image is significantly darker than the right side. The filtered image shows that the filtered image was able to remove this intensity difference without removing images of aggregates that are the focus of the study.

3.3 Local Histogram Equalization

The goal of this process is to increase the contrast of the images. The process is similar to the histogram specification procedure. However, whereas that process was applied globally, this process is localized to a specified mask size (60 pixels x 60 pixels). Also, instead of specifying a histogram to match to within each mask, the mask is equalized over the dynamic range of grayscale. [13] The results from this process are shown in Figure 3.4.



FIGURE 3.4: Local Histogram Processing

3.4 Binary Image

The image is then converted in a binary image. This is done by a threshold in ImageJ. Every pixel with an 8-bit value over 215 was converted to white (not an aggregate), and every pixel below that value was converted to black (an aggregate).

The results from this process are shown in Figure 3.5.

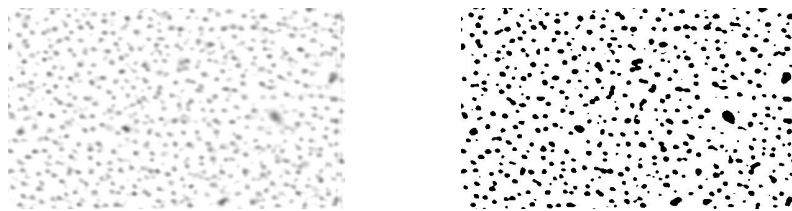


FIGURE 3.5: Binary Image Results

Chapter 4

DATA COLLECTION

After the image processing was completed, data was collected from the images. For each binary image, this included the size and location of each aggregate in the XY plane.

4.1 Statistical Analysis

Aggregates with sizes smaller than 5 pixels² were removed as outliers, because they are most likely artifacts of the image processing and not actually aggregates. The upper bound for outlier consideration was determined by a statistical analysis of the data. Outliers were aggregates which had a size twice the inter-quartile range above the third quartile. Therefore, this upper bound varied between images and depends on the distribution of the aggregates.

4.2 Number Density & Average Aggregate Size

For each image, the number density and average aggregate size were calculated. The number density was calculated by taking the total number of aggregates measured and dividing by the viewing dimension that was noted in Chapter 2.

The average size of the aggregates for each image was taken. The histogram in Figure 4.1 allows for a preliminary look at these quantities for a specific image.

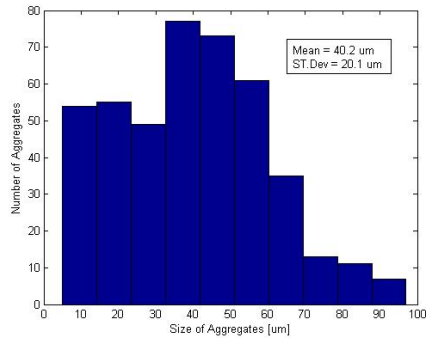


FIGURE 4.1: Histogram of Aggregate Size

4.3 Average Inter-Aggregate Spacing

The average inter-aggregate spacing was also analyzed. This data was collected via a delaunay triangulation algorithm using the locations of the center of each aggregate gathered from the ImageJ analysis. Delaunay triangulation is a triangulation such that no point lies within the circumcircle of any triangle. Figure 4.2 shows the triangulation superimposed on a binary image. The average length of the sides of the triangles is taken as the average inter-aggregate spacing.

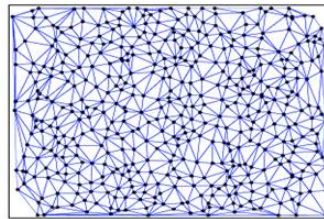


FIGURE 4.2: Delaunay triangulation

Chapter 5

KINETICS OF AGGREGATION

5.1 Observations

As described in experimental methods, a continuous field was applied to the sample and the evolution of chains into columnar aggregates was recorded in the ST-view. Initially, chains with small numbers of particles form, but these are difficult to distinguish in the images. At longer times, the system coarsens as the initial chains begin merging into larger ones. [3] As this process occurs, individual aggregates become visible, and quantitative data can be extracted from the images. The appearance of visible structures occurs approximately 200 seconds after the start of the magnetic field. The coarsening of these columnar aggregates continues as evident by their increase in cross-sectional area and inter-aggregate spacing and decrease in number density.

Qualitatively, the number density and inter-aggregate spacing show similar trends between trials. Comparing the data at varying field strength and constant time and volume fraction, higher field strengths give rise to higher number densities and smaller aggregate spacings, while smaller values of field strength show

the opposite trend. Similar trends are observed for different volume fractions at constant field strength and time. These trends are apparent in the InSPACE 1 data, but they are more prominent in the InSPACE 2 data, since both volume fraction and field strength are varied over a larger range of values. These trends are not unexpected. At higher values of field strength and volume fraction, the kinetics of aggregation should be faster, since particle interactions are stronger at higher field and the particles are initially in closer proximity to each other.

With regards to the average cross-sectional area, the values between experiments are the same order of magnitude, but the data is fairly scattered and does not lead to an obvious correlation between higher and lower field strength.

5.2 The Smoluchowski Equation

In order to provide context for the InSPACE experiments and provide a physical model for the kinetics of aggregation, the Smoluchowski kinetic equation for irreversible aggregation is reviewed. It was developed by Marian Smoluchowski, a contemporary of Einstein, and was originally applied to the coagulation of colloids.[14]

The Smoluchowski equation is an integro-differential equation. In Equation 5.1, the equation has been discretized. Therefore, the integrals have been reduced to summations over all chains.[14] The left hand side of this equation describes the time evolution of the number of chains of size s , n_s . These chains are also known as s -mers. The first term of the right hand side takes into account combination

reactions between i -mers and a j -mers to form s -mers, and the second represents the decrease in k -mers by the combination of s -mers with j -mers to form larger chains. The breakup of s -mers to smaller chains is not considered. All combination reactions are considered to be binary, with rate constants K_{ij} . This assumption makes the Smoluchowski equation only applicable at low chain concentrations.[3, 14]

$$\frac{dn_s(t)}{dt} = \frac{1}{2} \sum_{i+j=s} K_{ij}n_i(t)n_j(t) - n_s(t) \sum_{j=1}^{\infty} K_{kj}n_j(t) \quad (5.1)$$

In this equation, K_{ij} is the reaction kernel and gives the rate of coalescence of a chain size i with a chain size j . The lack of a disintegration term may also be justified by considering that this reaction kernel gives the net rate of chain formation. The reaction kernel can take on several different forms, and depending on this form leads to different solutions.[3]

K_{ij} is a product of a collision cross section term ($R_i + R_j$) and a diffusion coefficient term ($D_i + D_j$).[3] MR fluids have been shown to aggregate tip to tip. In this case, the collision cross section term should be unchanged with chain length. However, the diffusion coefficient will change with the number of particles in a chain.[3]

When the diffusion coefficient takes on a power law dependence the chain size, $D_i \sim i^\gamma$, K_{ij} takes the following form,

$$K_{ij} \sim i^\gamma + j^\gamma.[3] \quad (5.2)$$

When the reaction kernel described in Equation 5.2 is substituted into the Smoluchowski equation, at long times there is an emergence of a power-law distribution with an exponent that depends only on the diffusion coefficient of the chains. This is described in Equation 5.3, where $\langle s(t) \rangle$ is the mean chain length and $z = 1/(1 - \gamma)$. These theoretical predictions based on the physical Smoluchowski model have been supported by numerous previous works as well as numerical simulations.[15, 16]

$$\langle s(t) \rangle \sim t^z \tag{5.3}$$

Based on the Einstein relation for diffusion at low Reynolds number, given in Equation 5.4, the diffusion coefficient is inversely proportional to the size of the particle. This means that $D_i \sim i^{-1}$. Given this, it is expected that $\langle s(t) \rangle \sim t^{0.5}$. [3]

$$D = \frac{k_B T}{6\pi\eta a} \tag{5.4}$$

The quantitative kinetic data from the InSPACE experiments are analyzed using this model in the following sections.

5.3 Number Density of Aggregates

The above analysis of the Smoluchowski equation leads to the relationship found in Equation 5.3, where the average length or number of particles in a chain has a power-law dependence on time. The number density of aggregates, N , does not equal $\langle s(t) \rangle$, but it can be correlated to this quantity. Based on a conservation of

particles, the average size of a chain at a given time is simply the initial number of particles divided by the number of chains at that given time. This relationship is shown in Equation 5.5. Given this, the N versus time should also have a power law dependence but with an exponent of $-z$, shown in Equation 5.6.[15]

$$\langle s(t) \rangle = \frac{N_o}{N} \quad (5.5)$$

$$N \sim t^{-z} \quad (5.6)$$

5.3.1 InSPACE 1

The InSPACE 1 results for number density of aggregates versus time are shown in Figure 5.1. The data is plotted on a log-log plot, and at long times, the dependence on time is linear. The negative slope of these curve support the power law dependence described in Equation 5.5. The data shows that at small times, the power law dependence does not hold. This initial transient behavior is predicted by the Smoluchowski equation and has been observed in previous work.[3]

At times above the transition to power law dependence, the above curves were fit to a straight line. The slope of these lines corresponds to the exponent of $-z$. The values of z based on each experiment along with the R^2 correlation values for each fit are found in Table 5.1. The values for z are in the range of 0.25 to 0.40 for all experiments, and each fit has high correlation value. Other studies have found

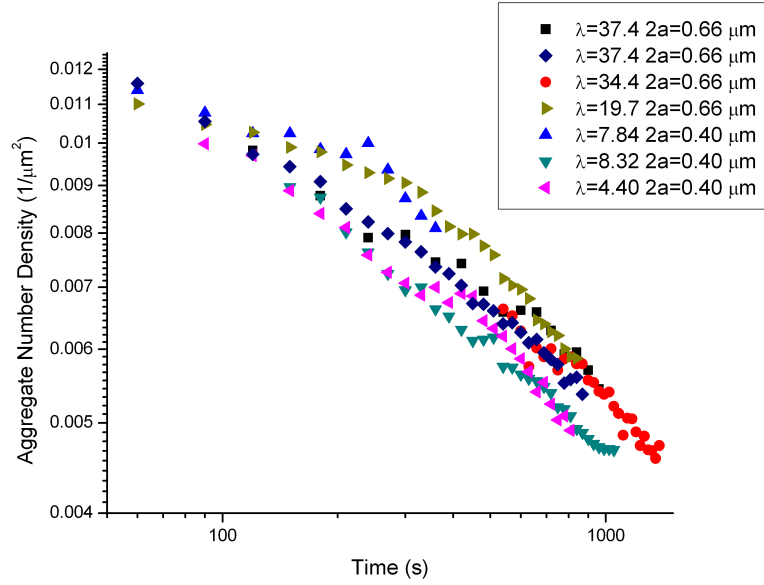


FIGURE 5.1: Number Density of Aggregates vs. Time - InSPACE 1

z for similar system to be around 0.3, which is in the middle of the range found here and compares well to many of these experiments.[17]

TABLE 5.1: Values of z from Number Density - InSPACE 1

$2a=0.66\mu\text{m}$			$2a=0.40\mu\text{m}$		
λ	z	R^2	λ	z	R^2
37.4	0.31	0.95	8.32	0.36	0.98
37.4	0.32	0.99	7.84	0.26	0.92
34.4	0.40	0.94	4.40	0.34	0.93
19.7	0.36	0.96			

5.3.2 InSPACE 2

The InSPACE2 experiments for number density of aggregates versus time are shown in Figure 5.2. The data is plotted on a log-log plot, and the dependence on time is linear. Again, the negative slope of these curves supports the power law

dependence described by Equation 5.5. There appears to be two sets of curves within this data and a transition between them. The experiments with $\lambda = 30.22$ are strongly negatively sloped, while the experiments with $\lambda = 120.9$ are nearly flat. The experiment with $\lambda = 68.00$ serves as a transition between the two types of curves.

Also, Some of the data shows an initial transient behavior before the power-law dependence develops. However, unlike InSPACE 1, where this was true for nearly every experiment, this only occurs in the experiments with lower values of λ and ϕ . This transition to power-law dependence is also less pronounced in InSPACE 2 than InSPACE 1. The experiments with higher values of λ and ϕ do not show this initial transient behavior. Previous work has shown that the transient behavior is more pronounced at low values of ϕ . These experiments support this previous observation, since the transient behavior was more pronounced in InSPACE 1 ($\phi=0.20\%$) and the low ϕ values of InSPACE 2. Additionally, these experiments suggest that there is a similar trend in λ for the degree to which transient behavior is observed and the time it takes power-law dependence to emerge.

The curves from the InSPACE 2 experiments, at times above the transition to power law dependence, were fit to a straight line, and the values for z based on each of the InSPACE 2 experiments were calculated. These along with the R^2 correlation values for each fit are tabulated in Table 5.2. The values are strikingly different from those observed in the analysis of InSPACE 1. With the InSPACE 1

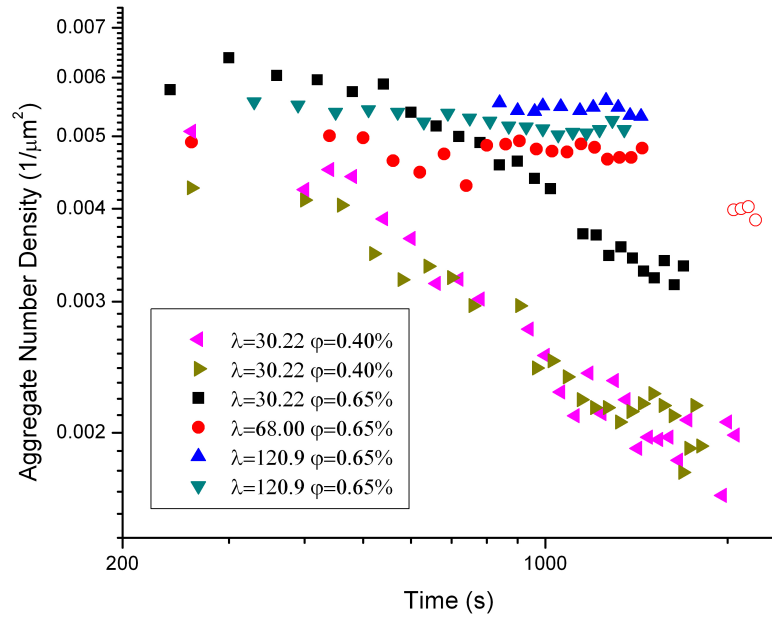


FIGURE 5.2: Number Density of Aggregates vs. Time - InSPACE 2

experiments, z values were all around 0.25 to 0.40, while InSPACE 2 values vary over an entire order of magnitude ($z = 0.58$ to 0.045). This supports previous work that z is both a function of λ and ϕ [3]. It should also be noted that the residual values (R^2) for these fits are not nearly as high as the InSPACE 1 experiments. While the residual values of experiments at lower values of λ are relatively high, (≥ 0.75), the accuracy of the fit decreases significantly as λ is increased. For example the highest λ of 120.9, one experiment yields an residual value of 0.85 while the other has a value of 0.39. Analysis of the values of z obtained and the shape of the curves, these curves show an extremely weak dependence on time. Any noise in the data will have a relatively high effect on the precision of the fit to such curves.

TABLE 5.2: Values of z from Number Density - InSPACE 2

ϕ	λ	z	R^2
0.40 %	30.22	0.58	0.91
0.40 %	30.22	0.51	0.94
0.65 %	30.22	0.40	0.90
0.65 %	68.00	0.10	0.60
0.65 %	120.9	0.045	0.39
0.65 %	120.9	0.085	0.85

Another point of interest is are the last 4 points of the trial with $\lambda = 68.00$, which are indicated on Figure 5.2 with hollow circles. These four points are significantly lower than from earlier in the experiment, and deviate from the linear trend established by the previous points. The ISS officer refocused the camera throughout the experiments in order to ensure accurate measurement, and at this point of this trial, the camera was focused on a different plane of view than the rest of the experiments. Based on the observation of the video, this plane of view is believed to be closer to the edges of the cell than that of the general experiment, as shown in Figure 5.3.

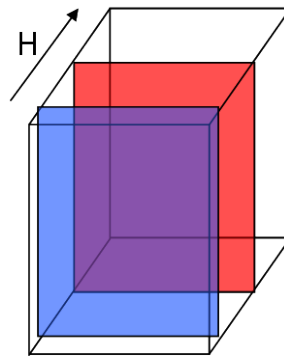


FIGURE 5.3: Visual representation of cell depth comparison

A comparison of two still images from this experiment are found in Figure 5.4. The image on the left comes from the middle the experiment where the plane of focus is the middle of the cell (shown in blue in the previous figure), and the image on the right is from the end of the experiment where the plane of focus has moved towards the edge of the cell (shown in red in the previous figure). As evident by the figure, the images are focused on two different planes. Based on this and the sudden jump down in number density, there appears to a larger number density of aggregates in the bulk of the material compared to that near the edges of the cell.

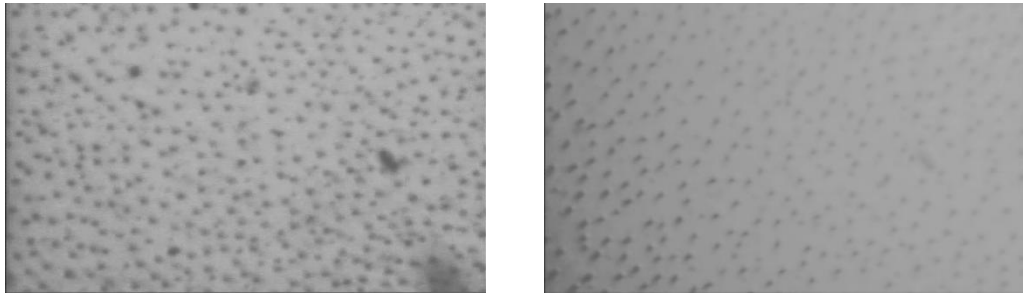


FIGURE 5.4: Plane of view comparison

5.4 Inter-aggregate Spacing

Next, we calculate the average inter-aggregate spacing. Like the number density of aggregates, the inter-aggregate spacing does not equal $\langle s(t) \rangle$, and does not scale exactly with t^z . However, it can be correlated to this quantity such that a value of z can be obtained. The average separation of chains, $\langle R \rangle$, is given by the relationship shown in Equation 5.7, where d is the dimensionality of the system. [18]

This equation can be verified simply using $\langle s(t) \rangle$ equal to 1 and a dimensionality equal to 3. This yields $\langle R \rangle \sim \phi^{-1/3}$, which give the scaling in three-dimensions of a colloidal mixture of single particles as function of ϕ . In order to relate Equation 5.7 to scaling factor that depends on z , the relationship that $\langle R \rangle$ scales with t^z is used. The dimensionality of this system is 2 since the focal plane is limited to a 2D plane, and ϕ is not evolving with time. Based on this method of analysis, the scaling of $\langle R \rangle$ with time is determined and shown in Equation 5.8.

$$\langle R \rangle \sim \left(\frac{\langle s \rangle}{\phi} \right)^{1/d} \quad (5.7)$$

$$\langle d \rangle \sim t^{\frac{z}{2}} \quad (5.8)$$

5.4.1 InSPACE 1

The InSPACE 1 experiments for inter-aggregate spacing versus time are shown in Figure 5.5. The data is plotted on a log-log plot, and at long times, the dependence on time is linear. The positive and smaller slope than the number density curves supports the power law dependence described in Equation 5.7. Like the number density data, this data shows that at short times, the power law dependence does not hold.

The values z based on Equation 5.8 were calculated for each experiment. These, along with the slope from which they were calculated and R^2 correlation values for each fit, are summarized in Table 5.3.

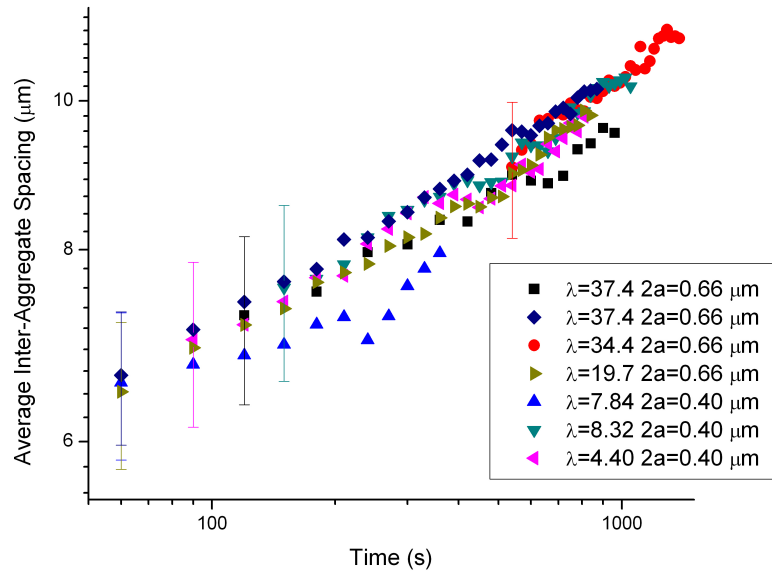


FIGURE 5.5: Average Inter-aggregate Spacing vs. Time - InSPACE 1

TABLE 5.3: Values of z from Inter-aggregate Spacing - InSPACE 1

$2a=0.66\mu\text{m}$				$2a=0.40\mu\text{m}$			
λ	slope	R^2	z	λ	slope	R^2	z
37.4	0.24	0.91	0.28	8.32	0.19	0.94	0.38
37.4	0.17	0.99	0.34	7.84	0.14	0.88	0.28
34.4	0.20	0.94	0.39	4.40	0.13	0.91	0.26
19.7	0.17	0.97	0.35				

5.4.2 InSPACE 2

The results of the InSPACE 2 experiments for inter-aggregate spacing versus time are shown in Figure 5.6. On a log-log plot, the linear dependence is consistent with the power-law described by equation 5.8.

Next, the values for z based on each of the InSPACE 2 experiments are calculated. These, along with the slope from which they were calculated and R^2 correlation values for each fit, are summarized in Table 5.4. The trends discussed

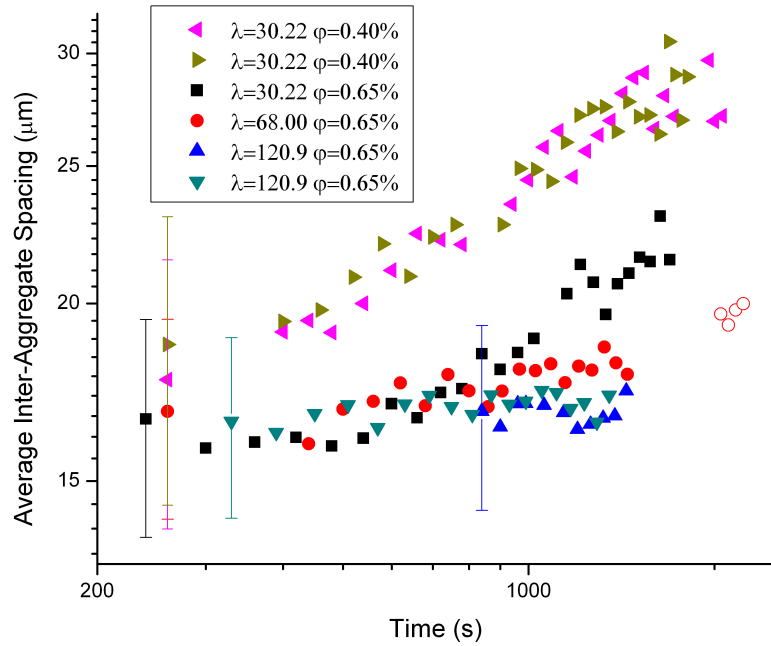


FIGURE 5.6: Average Inter-aggregate Spacing vs. Time - InSPACE 2

above for the number density are followed by this data as well, including the part concerning the 4 data point at the end of the trial with $\lambda = 68.0$. In the case of inter-aggregate spacing, these 4 data points deviate from the established long time behavior. Also of note, the residual square values for the highest values of λ are extremely low, much lower than those established for the number density analysis. Because of this, these values obtained for z are not used in further analysis.

TABLE 5.4: Values of z from Inter-aggregate Spacing - InSPACE 2

ϕ	λ	slope	R^2	z
0.40%	30.22	0.27	0.88	0.54
0.40%	30.22	0.27	0.92	0.54
0.65%	30.22	0.19	0.84	0.39
0.65%	68.00	0.074	0.63	0.15
0.65%	120.9	0.016	0.03	0.032
0.65%	120.9	0.025	0.19	0.049

5.5 Aggregate Cross-sectional Area

The results from the average cross-sectional area are presented in the following section. Unlike the number density of aggregates and the inter-aggregate spacing, the average cross-sectional area does not scale easily with a variation of t^z . Several assumptions have been made in order to arrive at scaling that correlates to the Smoluchowski exponent. If the aggregates are considered to have a circular cross-section, the average aggregate cross-sectional area, $\langle A \rangle$, should scale as the average radius squared, $\langle r \rangle^2$. The radius of the aggregate is dependent on the number of particles in the aggregate cross section and how those particles are structured in the cross section. For this analysis, the structure of the cross section is assumed to be hexagonally close packed, as shown in Figure 5.7.

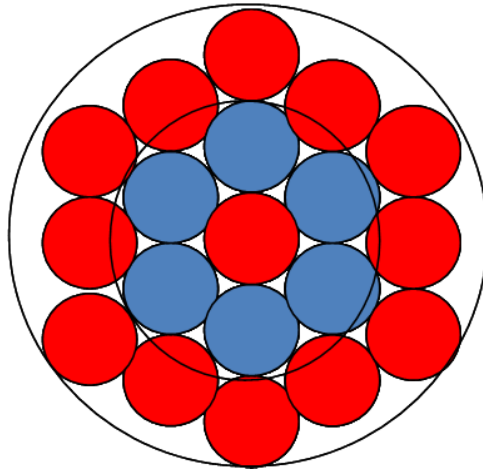


FIGURE 5.7: Hexagonal Cross Sectional Particle Structure with Circular Radius Representation

With these assumptions, equations which explain how the overall radius of the aggregate evolves as function the radius of an individual particle are obtained.

Equation 5.9 shows how the number of particles, s , in a cross section evolves as the number of layers in the hexagonal structure, x , changes. The one particle level is the zeroth layer. Equation 5.10 explains how the radius of the circular representation of the aggregate, r , evolves as function of the radius of a particle and the number of hexagonal layers added.

$$s = 1 + 6 \sum x \quad (5.9)$$

$$r = a(1 + 2x) \quad (5.10)$$

As the radius becomes larger, it takes increasingly more particles to expand the radius by a given amount. Thus, the radius does not scale directly as the number of particles, but rather as another power-law expression, say s^y . This will mean that $\langle A \rangle$ should scale as s^{2y} . Figure 5.8 shows the power law evolution following Equation 5.9 & Equation 5.10. This figure shows that given the assumptions used to derive the equations, y is approximately 0.5. Applying this value of y and that $\langle s \rangle$ scales as t^z , the average aggregate size should scale as t^z .

However, this model for scaling is only as good as the assumptions used to derive it. The assumptions that are most likely to break down are the circularity of the aggregates and the hexagonal close packed cross-sectional structure. If these do breakdown, the exponent for the scaling will not be directly applicable to the exponent z determined by the Smoluchowski equation.

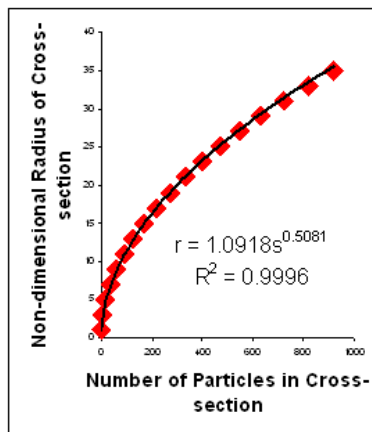


FIGURE 5.8: Radius of Cross Section as Function of Number of Particles

Also, average aggregate size is likely the least reliable of our measurements. It is the most sensitive measurement to the image processing techniques. Also, an imprecise alignment between the optical axis of the camera and the direction of the magnetic field of even a fraction of a degree will have significant effects on this measurement. If the camera that takes the straight on view is not perfectly aligned with the magnetic field, then the measured average aggregate size is enlarged because it reflects a growing length viewed obliquely. An exaggerated depiction of how this would look in both ST and RT view is shown in Figure 5.9. This not only makes the measurement inaccurate, but also makes it difficult to distinguish between the initial transient behavior of the Smoluchowski equation and an initial jump in the data due to obliquely measured area.

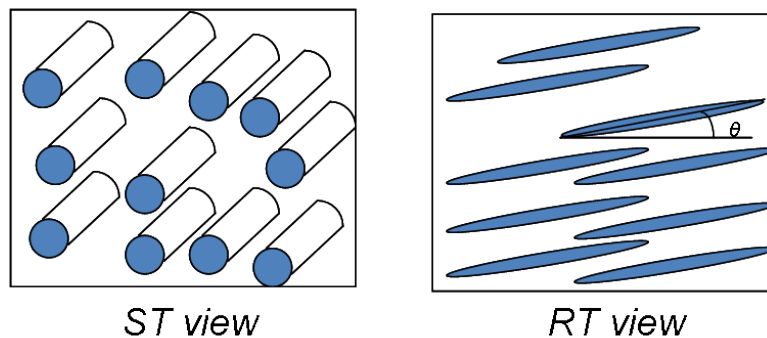


FIGURE 5.9: Exaggerated depiction of possible oblique cross-sectional measurements

5.5.1 InSPACE 1

The InSPACE 1 data for average cross sectional area versus time are shown in Figure 5.10. The data is plotted on a log-log plot, and the dependence on time is linear, suggesting a power law evolution.

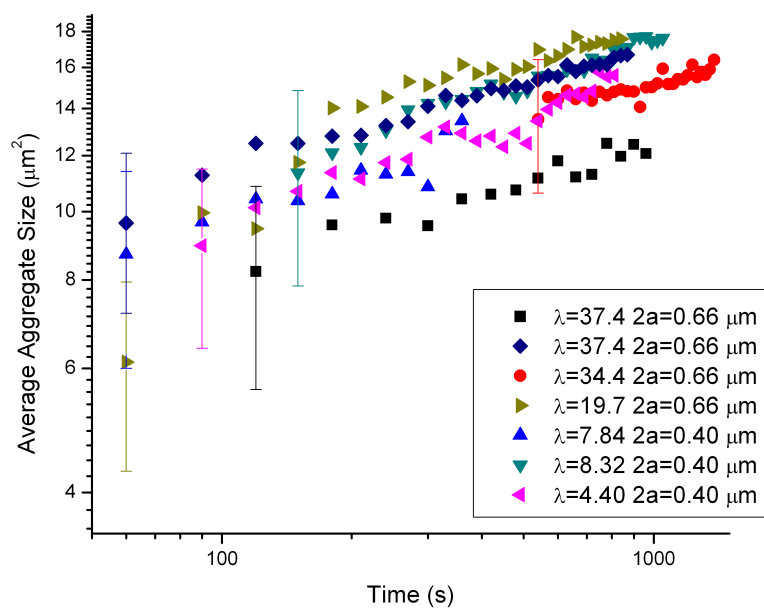


FIGURE 5.10: Average Cross-sectional Area vs. Time - InSPACE 1

The values for slope and R^2 correlation values for each fit are found in Table 5.5. These do not correlate with the z values found from the number density and inter-aggregate spacing.

TABLE 5.5: Power-law Dependence of Average Cross-sectional Area - InSPACE 1

2a=0.66 μ m			2a=0.40 μ m		
λ	slope	R^2	λ	slope	R^2
37.4	0.20	0.87	8.32	0.21	0.92
37.4	0.17	0.97	7.84	0.25	0.66
34.4	0.15	0.70	4.40	0.35	0.90
19.7	0.15	0.93			

5.5.2 InSPACE 2

The results of InSPACE2 experiments for average cross-sectional area versus time are displayed in Figure 5.11. The data is plotted on a log-log plot, and the dependence on time for one experiment ($\lambda = 30.22$ & $\phi = 0.65$ %) is strongly linear, supporting a power law dependence, but for most of the experiments the curves generated are nearly flat.

The values for the slope and R^2 correlation values for each fit are found in Table 5.6. Again, these values for the slope do not correlate with the values of z found in the number density and inter-aggregate spacing analysis.

The disagreement with the values of the slope from this analysis of the average cross-sectional area with the values of z found the number density and inter-aggregate spacing analysis shows that the assumptions made in the preliminary

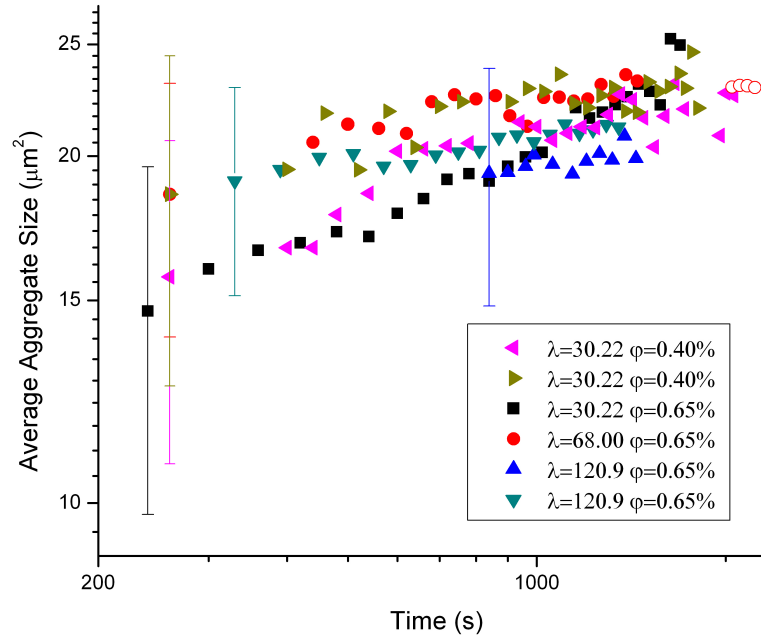


FIGURE 5.11: Average Cross-sectional Area vs. Time - InSPACE 2

TABLE 5.6: Power-Law Dependence of Average Cross-sectional Area - InSPACE 2

ϕ	λ	slope	R^2
0.40%	30.22	0.087	0.53
0.40%	30.22	0.12	0.67
0.65%	30.22	0.25	0.95
0.65%	68.00	0.023	0.38
0.65%	120.9	0.040	0.42
0.65%	120.9	0.085	0.80

analysis for the evolution of average cross-sectional area break down. However, despite the breakdown of these assumptions, a power law dependence for average cross-sectional area is still observed for most experiments. This is because the principle that it takes increasingly more particles to expand the average radius of the cross-section by a given amount is still true. Thus the average radius of an

aggregate still scales as power-law expression, but the y value is not 0.5.

5.6 Discussion

5.6.1 Values of z comparison

As discussed before, in diffusion limited aggregation with a diffusion coefficient based on the Equation 5.4, z should attain a value of 0.5. The analysis of the data using the Smoluchowski equation gives varying values of z based on different experimental parameters. This variability in z with ϕ and λ has been observed in previous work. [3] The comparison of the values of z between the methods of analysis for number density and inter-aggregate spacing is shown in Table 5.7 and Table 5.8. With the exception of a few trials, the values are in good correlation with each other. In InSPACE 1, z values for each experiment are within experimental error of each other, with the exception of the lowest value of lambda ($\lambda = 4.40$). In this experiment, the value of z obtained from the spacing analysis is significantly smaller than that determined from the number density analysis. In InSPACE 2, z values for each experiment are again within experimental error of each other with the exception of one experiment. The experiment of with $\lambda = 68.00$ and $\phi = 0.65\%$ has a big deviation between the two values of z . This can be partially explained by the change in focus throughout this experiment.

As discussed in chapter 1, the kinetics of aggregation are sensitive to both ϕ and λ . In order to compare experiments with varying parameters (a, ϕ , and

TABLE 5.7: z Comparison - InSPACE 1

2a=0.66 μ m			2a=0.40 μ m		
λ	$z_{numberdensity}$	$z_{spacing}$	λ	$z_{numberdensity}$	$z_{spacing}$
37.4	0.31	0.28	8.32	0.36	0.38
37.4	0.32	0.34	7.84	0.26	0.28
34.4	0.40	0.39	4.40	0.34	0.26
19.7	0.36	0.35			

TABLE 5.8: z Comparison - InSPACE 2

ϕ	λ	$z_{numberdensity}$	$z_{spacing}$
0.40%	30.22	0.58	0.54
0.40%	30.22	0.51	0.54
0.65%	30.22	0.40	0.39
0.65%	68.00	0.10	0.15
0.65%	120.9	0.045	0.031
0.65%	120.9	0.085	0.049

λ), the values of z for InSPACE 1 and InSPACE 2 are compared against two characteristic length scales r_c^{max} , the maximum distance at which the dipole-dipole interaction energy is equal to the energy of the thermal fluctuations, and r_o , the initial particle separation. In order to facilitate this comparison, the values of z are plotted versus r_c^{max}/r_o . The ratio of these two length scales allows us to distinguish between diffusion-limited and field driven aggregation processes (i.e. when this ratio is greater than 1, then the process is field driven). [18]

Figure 5.12 shows the results of this analysis for InSPACE 1. Although there is no real correlation between values of z and this ratio, the value of ratio shows that the processes in these experiments are diffusion-limited. Figure 5.13 shows the results of this analysis for InSPACE 2. This figure shows a decreasing trend in the

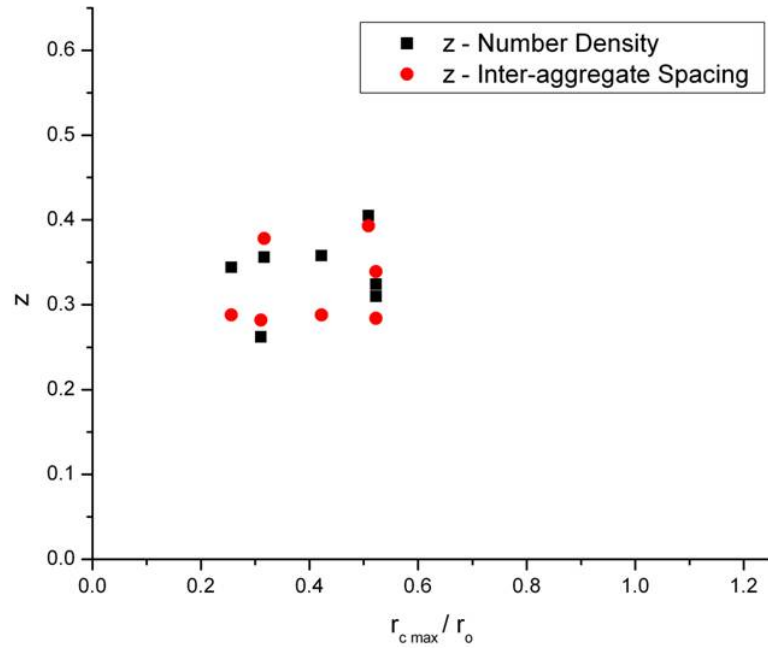


FIGURE 5.12: z vs. characteristic length ratio - InSPACE 1

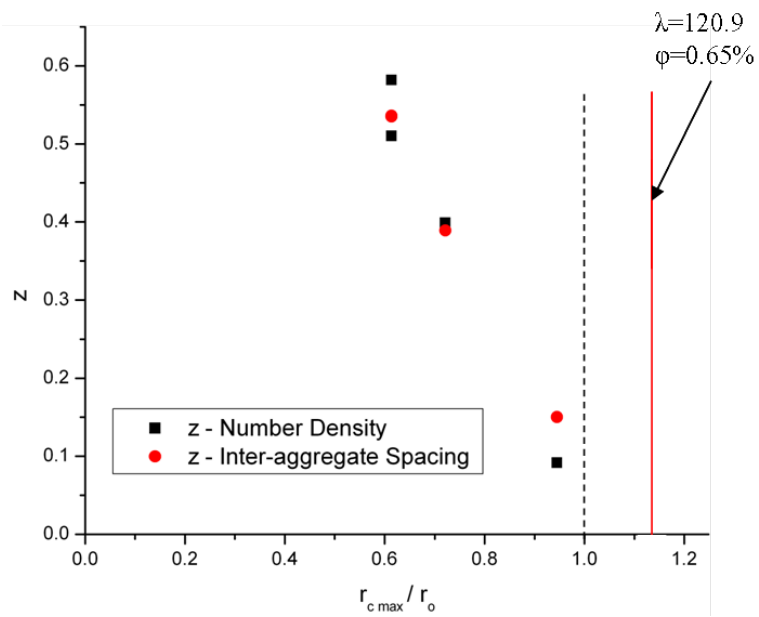


FIGURE 5.13: z vs. characteristic length ratio - InSPACE 2

value of z with an increase in the r_c^{max}/r_o . It difficult to tell exactly what type of function this decrease follows due to scatter and that their are only 6 experiments. However, the value for z appears to decay towards 0. Another point of interest in this figure is that the highest values of λ correspond to an r_c^{max}/r_o ratio greater than 1, which dictates that the processes here are field driven aggregation. This may correspond to the flatness of the curves found in the kinetic data for these high values of λ .

5.6.2 Dynamic Scaling Theory

The strong agreement in the values of z shows the ability of the Smoluchowski model to describe the kinetics of aggregation of MR fluids, but it also gives more insight into the methods of aggregation. These values of z are determined by analysis of the number of aggregates and the average inter-aggregate spacings, and these two methods of analysis are equivalent only under certain conditions. $\langle s \rangle \sim t^z$ still holds. Therefore, based on the methods of analysis in Section 5.4, the z determined for the inter-aggregate spacing is the z predicted by the Smoluchowski equation. But, it has been shown that Equation 5.6 only to hold under certain conditions. [17, 18]

Dynamic scaling theory states that the number of chains of a given particle mass evolves with time is shown in Equation 5.11, where $w = z\Delta$ and $\tau = 2 - \Delta$. [17, 18]

$$n_s(t) \sim t^{-w} s^\tau f(s/t^z) \quad (5.11)$$

Summation of Equation 5.11 over all chain sizes leads to Equation 5.12. This shows that the exponent z' is only equal to the z derived from the Smoluchowski equation if $\tau < 1$.

$$N \sim t^{-z'} \equiv \begin{cases} t^{-z} & \text{for } \tau < 1 \\ t^{-w} & \text{for } \tau > 1 \end{cases} \quad (5.12)$$

In the case when the diffusion coefficient, D_s , for a cluster of mass s is given by $D_s \sim s^\gamma$, where γ is the diffusion exponent, theoretical predictions for the crossover exponent, Δ , have been determined. These are displayed in Equation 5.13.

$$\Delta = \begin{cases} 2 - \tau & \text{for } \gamma > \gamma_c \\ 2 & \text{for } \gamma < \gamma_c \end{cases} \quad (5.13)$$

The critical value of the diffusion exponent, γ_c , is the point at which aggregation dynamics changes from being dominated only by the large cluster small cluster interactions (below γ_c) to dynamics where large-small and large-large clusters interactions are equally important (above γ_c). [19, 20]

The good correlation between the values of z in Table 5.7 and Table 5.8 shows important things. It shows that the number density and inter-aggregate spacing decay and grow at the same rate. Also, because $z' = z$, τ must be less than 1 in order to satisfy Equation 5.12. Given this, Δ must be greater than 1. As shown by Equation 5.13, dynamic scaling theory assigns physical meaning to the values

of Δ . Given that Δ is greater than 1 and z is equal for inter-aggregate spacing and number density, both small-large and large-large aggregate interactions are important in the aggregation kinetics. In other words, the first statement of Equation 5.13 holds, and γ is greater the critical value. The one exception to this is the experiment in InSPACE 1 with $\lambda = 4.40$. As stated before, the value of z obtained in this experiment from the spacing analysis is significantly smaller than that determined from the number density analysis. This means that the number density was decaying faster than the aggregates were separating; therefore, in this case the small-large aggregation combination is more important.

Chapter 6

TIME SCALING OF KINETIC RESULTS

6.1 Time Scaling

This chapter deals with a proposed time scaling of the data, which allows for dimensionless analysis of the assembly kinetics. The non-dimensionalized analysis of time should allow all plots versus time to collapse together to form a single master curve, regardless of the experimental conditions. This will allow experiments with varying values of λ , ϕ , and particle radius to be compared.[3]

The proposed scaling stems from the characteristic time for doublet formation in a dilute system exhibiting purely Brownian motion. The particles join when they come in contact. This characteristic time is shown in Equation 6.1, where D is as defined in Equation 5.4.[3]

$$t_B = \frac{a^2}{6D\phi} \quad (6.1)$$

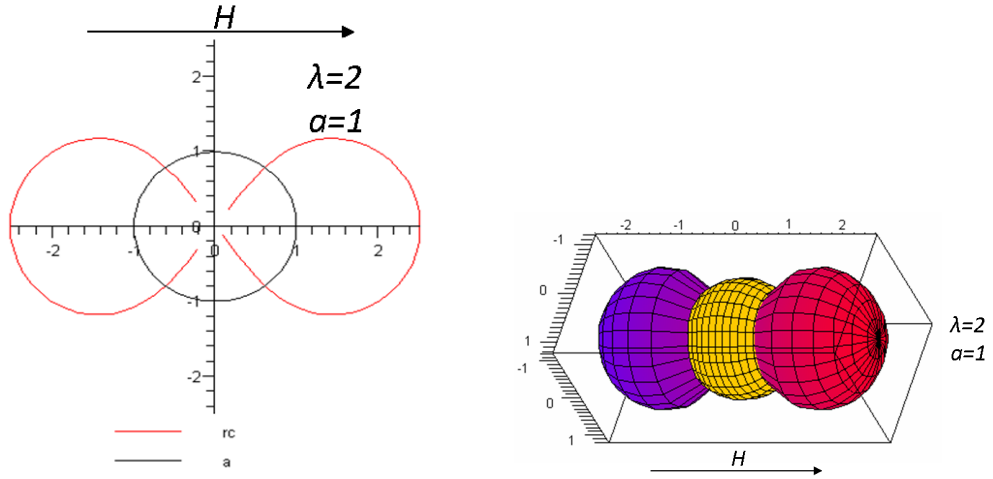
However, the particles in this system do not exhibit only Brownian motion, they also have induced dipoles due to the magnetic field. This results in two

aggregation time scales. When the particles are far away from each other, they diffuse by Brownian motion because the thermal energy dominates. But when this random diffusion brings particles in close enough contact, the dipole interaction overcomes the thermal energy. When this occurs, the particles exhibit a rapid transition to ballistic motion, and they aggregate immediately. This shows that the aggregation process is diffusion limited, since it is the rate limiting step in the aggregation of particles.[3]

Following the argument above, each particle can then be said to have a capture volume where this transition from random to ballistic motion will occur. The critical interaction energy is found at $\lambda=1$, shown in Equation 6.2, and the radius corresponding to this critical interaction energy, r_c , is shown in Equation 6.3. As seen in Equation 6.3, the capture volume will be a function of λ , a , and θ . A depiction of how θ affects r_c is shown in Figure 6.1. The only time that r_c exceeds a is at the tips of the particle that are in line with the field H . This supports the concept of tip to tip aggregation. [3]

$$\lambda = \frac{U(r_c)}{kT} = 1 \tag{6.2}$$

$$r_c = [4(3\cos^2(\theta) - 1)]^{\frac{1}{3}} a \lambda^{\frac{1}{3}} \tag{6.3}$$


 FIGURE 6.1: r_c as a function of θ

As shown in the 3-dimensional part of Figure 6.1, effective volume fraction of the particles is increased as result of the dipole interaction. The orange part of the figure is the original particle volume, the blue part is the positive part of the dipole, and the red part is the negative part of the dipole. The effective volume fraction, which includes this extended volume induced by the dipole, can be calculated from Equation 6.4.[3]

$$\phi_{eff} = 4 \left[\left(\frac{1}{3} \right)^{\frac{1}{2}} - \left(\frac{1}{3} \right)^{\frac{3}{2}} \right] \lambda \phi \quad (6.4)$$

This can then be used in Equation 6.1 to get at time scaling that takes into consideration the dipolar interaction between particles. In this study, that characteristic time is denoted t^* and is found in Equation 6.5. Once time is scaled by the characteristic time, t^* , the curves should collapse from several curves onto a

single master curve, from which deviations can be further analyzed.

$$t^* = \frac{a^2}{24 \left[\left(\frac{1}{3}\right)^{\frac{1}{2}} - \left(\frac{1}{3}\right)^{\frac{3}{2}} \right] D\lambda\phi} \quad (6.5)$$

6.2 InSPACE 1

Results from time scaling for InSPACE 1 are shown below. As seen by a comparison of these figures with figures from Chapter 5, some collapse occurs, but there is no single master curve. This phenomenon could possibly be due to an initial step in aggregation that involves nucleation of chains, but it may just be an imaging artifact due to the limited focal plane. A nucleation step in the aggregation will be investigated in further detail.

However, looking at the number density of aggregates shown in Figure 6.2, higher values of λ ($\lambda > 19.8$) seem to collapse relatively well, while the lower values of λ ($\lambda < 8.32$) do not collapse well. This could suggest that the model for t^* breaks down at small values of λ . One reason may be an initial generation of aggregates, or nucleation step of aggregation, is not considered in the model. If the number of aggregates was shifted by an initial number of nucleates, a master curve could probably be generated.

With regards to inter-aggregate spacing shown in Figure 6.3, similar conclusions to that of number density can be made. Some values of λ can be seen to collapse, but others show deviations. Similar to number density, the higher values appear

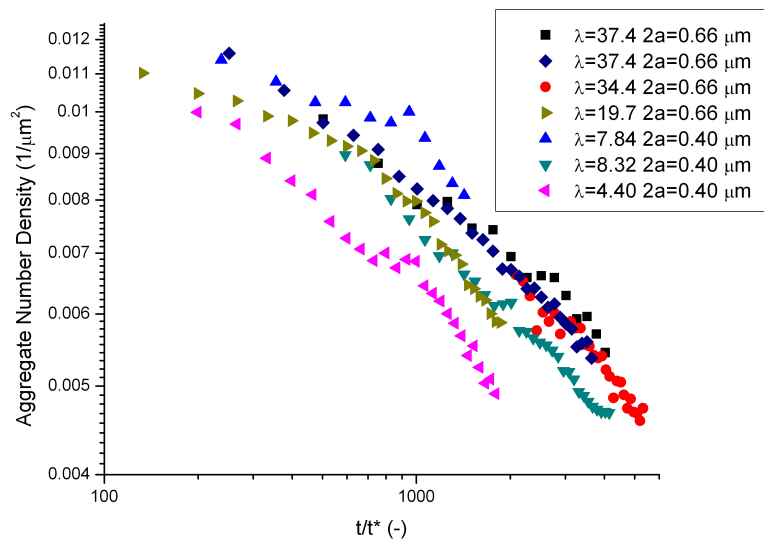


FIGURE 6.2: Number Density of Aggregates vs. t/t^* - InSPACE 1

to collapse well, and lower values appear to deviate more, but that is not always the case. This could be an artifact of the method of finding the separation as well as the initial number of nucleates.

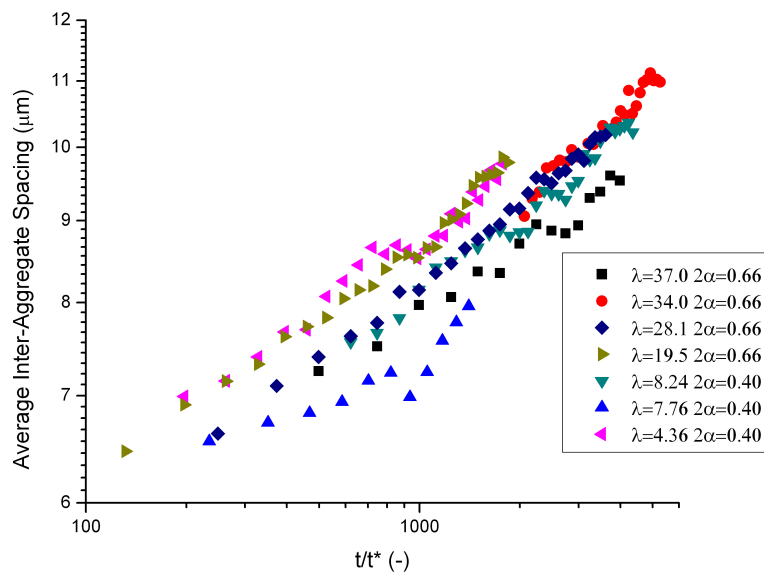


FIGURE 6.3: Average Inter-aggregate Spacing vs. t/t^* - InSPACE 1

Looking at aggregate area versus time shown in Figure 6.4, there seems to be no correlation between values of λ like the previous examples. This follows with the analysis performed in Chapter 5.

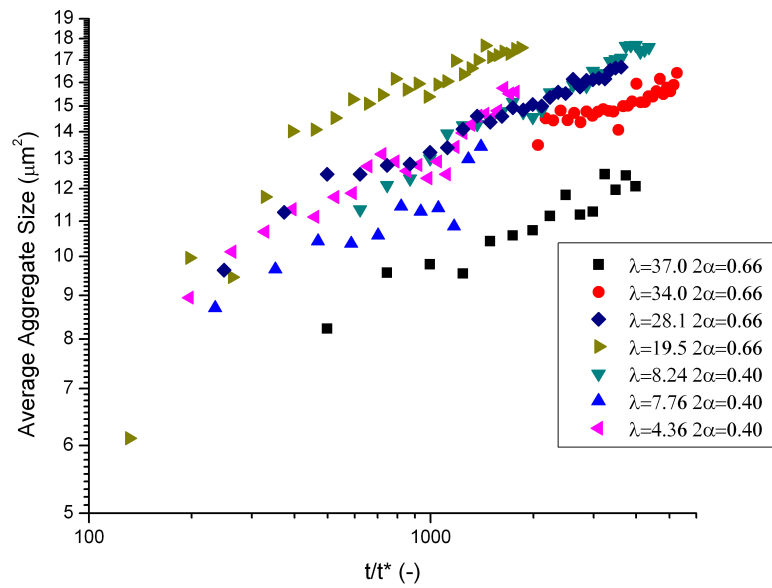


FIGURE 6.4: Average Cross-sectional Area vs. t/t^* - InSPACE 1

6.3 InSPACE 2

Results from time scaling for InSPACE 2 are shown in the following figures. Unlike the InSPACE 1 time-scaling results, these results show no collapse to a master curve. However, the results do show some potential for collapse. The data at low dimensionless times (low values of λ and ϕ) all exhibit fast or steep growth, and the data at higher dimensionless time (high values of λ and ϕ) show a shallow or slow growth with time. If these quantities, number density and average aggregates size were able to be shifted vertically, the curves could collapse. This vertical shift would be possible if there were scaling based on initial nucleation.

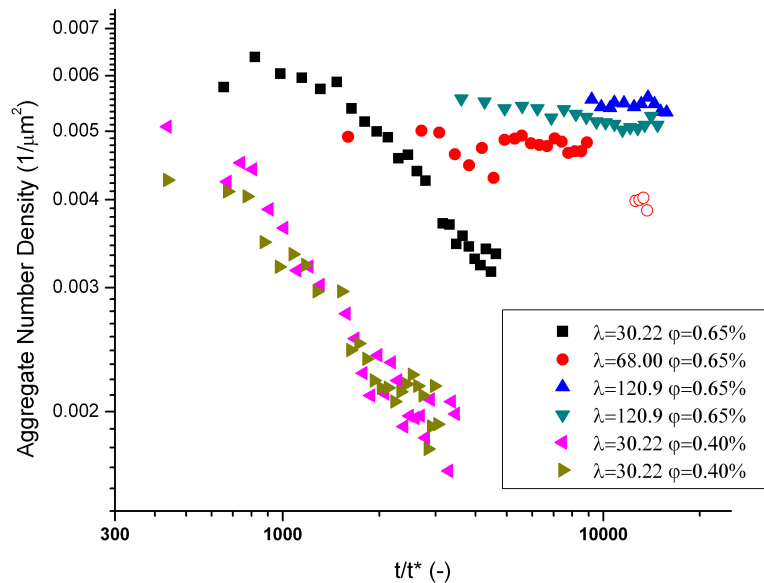


FIGURE 6.5: Number Density of Aggregates vs. t/t^* - InSPACE 2

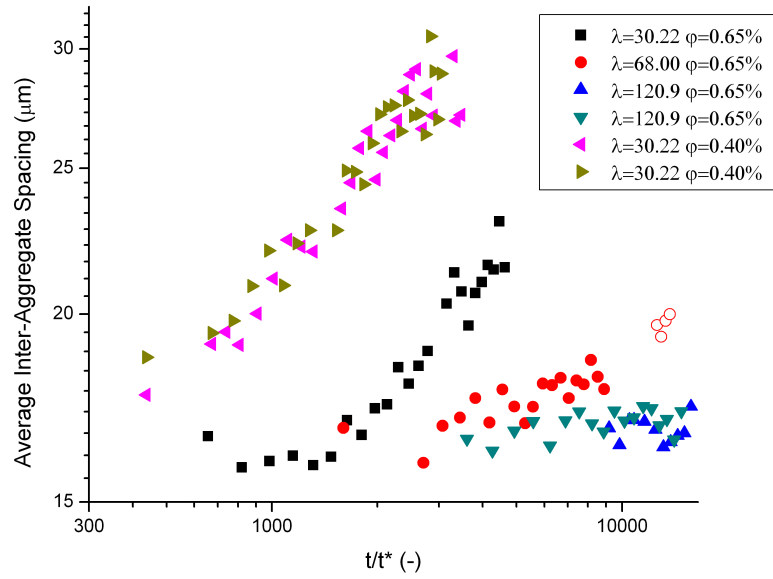


FIGURE 6.6: Average Inter-aggregate Spacing vs. t/t^* - InSPACE 2

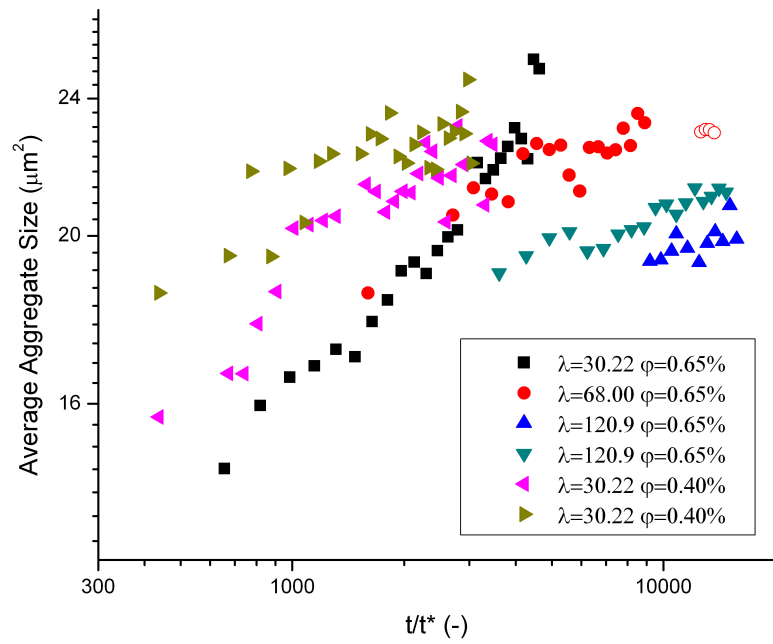


FIGURE 6.7: Average Cross-sectional Area vs. t/t^* - InSPACE 2

6.4 Nucleation Step of Aggregation

In the formation of chains, the contribution from enthalpy change is favorable. However, the entropy contribution is always unfavorable. This could lead essentially to an activation barrier, where chains with fewer particles than x are unstable as shown in Figure 6.8. However, as more particles are added to a chain, mutual induction and long-range interactions provide stability. This effect could affect the number of nucleates that are formed initially. Therefore, it becomes easier to add small aggregates to larger aggregates that are already stable. This initial number of nucleates would be a function of both ϕ and λ .

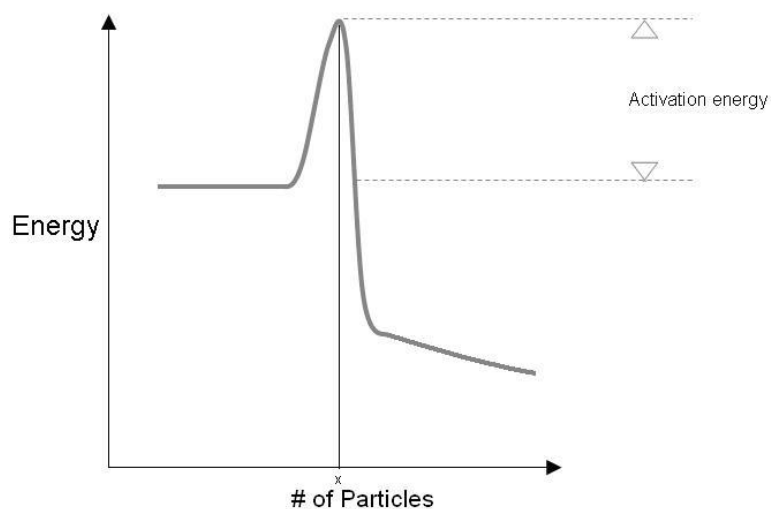


FIGURE 6.8: Representation of proposed activation barrier to aggregation

Chapter 7

CONCLUSIONS

- Background

The background about MR fluids, including properties and parameters as well as practical applications, were reviewed and discussed. The most important parameters for determining the structure and aggregation kinetics are ϕ and λ . The motivations of the thesis are outlined as the study of the long time aggregation kinetics of MR fluids under microgravity conditions.

- Experimental Methods

The details of the experimental procedure were outlined. The experiments were performed in the MSG on the ISS. InSPACE 1 varied the parameters of a and λ and held ϕ constant at 0.20 %, while InSPACE 2 varied the parameters of ϕ and λ and held a constant at 1.05 μm .

- Image Processing

Image processing techniques were used to clean the raw video microscopy. First, the images were pre-processed and intensity differences were removed.

The image was then passed through a series of filters and other image processing procedures to remove noise and enhance contrast.

- Data Collection

Data about the number density, inter-aggregate spacing, and average cross-sectional area were extracted from each processed image. This was done through a series of particle tracking algorithms. Statistical analysis on this data was performed to remove any outliers that survived the image processing techniques.

- Kinetics of Aggregation

The data of number density, inter-aggregate spacing, and average cross-sectional area were plotted and analyzed against time. This data was found to follow a power law dependence on time as predicted by the Smoluchowski equation for irreversible colloidal aggregation. The values of z determined for InSPACE 1 were all nearly around 0.30, while the values for InSPACE varied from 0.03 to 0.58 as functions of λ and ϕ .

- Time-Scaling

The kinetic data was scaled by a time constant and was plotted against non-dimensional time. The time constant is a function of both ϕ and λ , allowing experiments with varying parameters to be compared more readily. The data should have collapsed into a single master curve. However, this

did not occur. For InSPACE 1, there is relatively good collapse for most values of λ , but the model breaks down at low λ . For InSPACE 2, there is no collapse. The lack of collapse in the low values of λ for InSPACE 1 and the experiments of InSPACE 2 gives rise to a possible nucleation step in the aggregation process.

Bibliography

- [1] Ronald G. Larson. *The Structure and Rheology of Complex Fluids*. Oxford University Press, 1999.
- [2] Thomas B. Jones. *The Electromechanics of Particles*. Cambridge University Press, 1995.
- [3] A.P. Gast, J. Promislow, and M. Fermigier. Aggregation kinetics of paramagnetic colloidal particles. *J. Chem. Phys.*, 102(13), 1995.
- [4] A. P. Gast and E. M. Furst. Dynamic and lateral interaction of dipolar chains. *Physical Review E*, 62(5), 2000.
- [5] A. P. Gast and E. M. Furst. Micromechanics of magnetorheological suspensions. *Physical Review E*, 61(1), 2000.
- [6] A. P. Gast and J. Promislow. Magnetorheological fluid structure in a pulsed magnetic field. *Langmuir*, 12(17), 1996.
- [7] T. Phillips and P.L. Barry. Magnetic fluids. 2002. URL http://science.nasa.gov/headlines/y2002/23aug_MRfluids.htm.

- [8] J. David Carlson. Magnetorheological fluid damping. February 2002. URL <http://archives.sensorsmag.com/articles/0202/30/main.shtml>.
- [9] A. P. Gast and J. Promislow. Low-energy suspension structure of magnetorheological fluid. *Physical Review E*, 56(1), 1995.
- [10] Clayton T. Crowe. *Multiphase Flow Handbook*. CRC Press, 2006.
- [11] A. P. Gast and E. M. Furst. Micromechanics of dipolar chains using optical tweezer. *Physical Review Letters*, 82(20), 1999.
- [12] R.C. Gonzalez and R.E. Woods. *Digital Image Processing*. Prentice Hall, 1992.
- [13] Theo Schouten. Image enhancement. 2003. URL <http://www.cs.ru.nl/~this/rt2/col/h4/4verbeteringenENG.html>.
- [14] M. von Smoluchowski. *Z. Phys*, 17, 1916.
- [15] M. Kolb. Unified description of static and dynamic scaling of kinetic cluster formation. *Physical Review Letters*, 53(17), October 1984.
- [16] S. Miyazima, P Meakin, and F. Family. *Physical Review A*, 36, 1987.
- [17] J. Cernak, G. Helgesen, and A.T. Skjeltorp. Aggregation dynamics of non-magnetic particles in a ferrofluid. *Physical Review E*, 70, 2004.

- [18] P. Dominguez-Garcia, S. Melle, J.M. Pastor, and M.A. Rubio. Scaling in the aggregation dynamics of a magnetorheological fluid. *Physical Review E*, 76, 2007.

- [19] T. Vicsek and F. Family. Dynamic scaling for aggregation clusters. *Physical Review Letters*, 52(19), May 1984.

- [20] P. Meakin, T. Vicsek, and F. Family. Dynamic cluster-size distribution in cluster-cluster aggregation: Effects of cluster diffusivity. *Physical Review B*, 31(1), January 1985.

Appendix A

INSPACE DATA CATALOG

The catalogs for the ST and RT Views of InSPACE 1 are presented below. The cassette IDs are given for each experiment. The overall time for each cassette is given. In order to conserve DV cassettes on the ISS, some data was gathered via time-lapsed recording. The recording tab in the table distinguishes between continuous and time-lapsed recording. The field tab indicates pulsed or steady field. As stated before, this thesis focused only on steady field aggression. The observation tab indicates general qualitative comments from the experiment.

A.1 InSPACE 1 - ST View

Cassette ID 100

	<i>Time (min)</i>	<i>Recording</i>	<i>Field</i>	<i>Observations</i>
Total time	0:00-0:33	Continuous	-	dark
49:45 min	0:33-3:05	Continuous	Steady	aggregation into circular periodic structure
Notes	3:05-4:00	Continuous	Pulsed	dark
extra time @ end	4:00- 42:23	Continuous	Pulsed	aggregation into circular periodic structure w/ larger structures forming (semi out of focus)
	42:23-49:45	Time-Lapse	Pulsed	collection on larger particles, some wall shots with larger structures
	49:12-49:45	Time-Lapse	Pulsed	darker larger object of circular nature/ out of focus

Cassette ID 101

	<i>Time (min)</i>	<i>Recording</i>	<i>Field</i>	<i>Observations</i>
Total time	0:00-0:56	Continuous	-	dark
55:05 min	0:56-1:13	Time-Lapsed	Steady	small periodic circular columns
Notes	1:13-1:38	Continuous	Pulsed	dark
	1:38-37:50	Time-Lapsed	Pulsed	many small structures with interspersed larger ones, larger ones show growth over time, ejection and addition
	37:50-55:05	Time-Lapsed	Pulsed	walls shots with finger like structures, ejections and addition similar to free large structures

Appendix A. *InSPACE* Data Catalog

Cassette ID 101B

	<i>Time (min)</i>	<i>Recording</i>	<i>Field</i>	<i>Observations</i>
Total time	0:00-0:34	-	-	dark
52:10 min	0:34-1:04	Time-Lapsed	Steady	larger structures with groupings of smaller structures and periodic structure, picture fades to dark when pulsed field is applied
Notes	1:04-52:10	-	-	dark, seems to lighten up as time progresses but not enough to complete view structures

Cassette ID 104

	<i>Time (min)</i>	<i>Recording</i>	<i>Field</i>	<i>Observations</i>
Total time	0:00-1:27	Continuous	-	dark
55:04 min	1:27-2:56	Continuous	Steady	growth of small aggregates, drifts in and out of focus
Notes	2:56-22:57	Continuous	Steady	wall shots, pans from right wall to left (several times), darker near walls, right distinctively darker than the left
	22:57-46:36	-	-	dark, begin to lighten as time goes on but not enough to visibly ID most structures
	46:36-53:29	Continuous	Steady	wall shots, mostly right wall
	53:29-55:04	Continuous	Pulsed	wall w/ aggregates attached fades to dark

Appendix A. *InSPACE* Data Catalog

Cassette ID 105

	<i>Time (min)</i>	<i>Recording</i>	<i>Field</i>	<i>Observations</i>
Total time	0:00-0:57	Continuous	Steady	dark
52:41 min	0:57-13:32	Continuous	Steady	wall, darker near wall, small aggregates, pans from wall to wall, columns acculate into to tower like structures on the wall
Notes	13:32-18:01	Continuous	Pulsed	dark, still able to distinguish some structures @ beginning and end
	18:01-20:57	Continuous	Pulsed	growth of larger structures
	20:57-35:27	Time-Lapsed	Pulsed	wall, larger congregate on wall, ejection & addition
	35:27-35:32	-	Pulsed	dark
	35:32-52:41	Time-Lapsed	Pulsed	wall and larger structures show ejection and areas of depletion surrounding, smaller towers (fingers) towards end of segment

Cassette ID 105B

	<i>Time (min)</i>	<i>Recording</i>	<i>Field</i>	<i>Observations</i>
Total time	0:00-4:20	Continuous	-	dark, background shapes
54:53 min	4:20-20:03	Continuous	Steady	wall shots, a few large structures, several smaller structures
Notes	20:03-38:29	-	Pulsed	dark, some background shapes
	38:29-42:49	Continuous	Steady	wall shots w/ larger structures, pans from wall to wall, a few medium snake-like structures with periodic small structures in-between
	42:49-54:53	Continuous	Pulsed	dark, some background shapes, areas of depletion are last to go dark

Appendix A. *InSPACE* Data Catalog

Cassette ID 106

	<i>Time (min)</i>	<i>Recording</i>	<i>Field</i>	<i>Observations</i>
Total time	0:00-0:29	Continuous	Steady	dark
42:29 min	0:29-1:53	Continuous	Steady	periodic circular structures with w/ a concentration band next to wall
Notes	1:53-2:12	Continuous	Steady	finger like wall structures
	2:12-3:16	Continuous	Steady	periodic circular structures
	3:16-15:31	Continuous	Steady	finger like wall structures, periodic circular structures
	15:31-21:38	Continuous	Pulsed	fingers start to give way to larger structures
	21:30-22:07	Continuous	Pulsed	wall, ejection from & addition to larger structure
	22:07-31:03	Time Lapsed	Pulsed	wall, ejection from & addition to larger structure
	31:03-35:00	Time Lapsed	Pulsed	migration of larger structures to- wards walls
	35:00-38:10	Time Lapsed	Pulsed	Ejection of fingers from wall struc- tures
	38:10-39:59	Time Lapsed	Steady	large structures with large areas of depletion, fingers extending from wall
39:59-42:29	Time Lapsed	Pulsed	initially growth of fingers fades to black	

Appendix A. *InSPACE* Data Catalog

Cassette ID 106 - Steady

	<i>Time (min)</i>	<i>Recording</i>	<i>Field</i>	<i>Observations</i>
Total time	0:00-0:27	Continuous	Steady	central shot with many small circular structures w/ interspersed darker spots (noise?)
12:36 min	0:27-0:35	Continuous	Steady	left wall shot - very dark
Notes	0:35-2:55	Continuous	Steady	right wall shot - periodic structures become elongated and finger like
	2:55-3:20	Continuous	Steady	panning central shot - same as before except structures bigger
	3:20-4:07	Continuous	Steady	right wall shot - same as before
	4:07-6:03	Continuous	Steady	panning central shot w/ some left wall shots- same as before except structures bigger
	6:03-11:34	Continuous	Steady	right wall shot - same
	11:34-11:51	Continuous	Steady	panning central shot - same as before except structures bigger
	11:51-12:36	Continuous	Steady	right wall shot - same

Cassette ID 107

	<i>Time (min)</i>	<i>Recording</i>	<i>Field</i>	<i>Observations</i>
Total time	0:00-0:45	-	-	dark
55:05 min	0:45-1:53	Continuous	Steady	out of focus
Notes	1:53-14:58	Continuous(?)	Steady	circular periodic structures that evolve in size w.r.t. time (small= ϵ , large)
	14:58-39:13	-	Pulsed	picture goes dark in the first few seconds of pulsed field
	39:13-43:42	Continuous	Steady	circular periodic structures w/ with irregularly interspersed larger circular structures
	43:42-55:05	-	Pulsed	picture goes dark in the first few seconds of pulsed field

Appendix A. *InSPACE* Data Catalog

Cassette ID 108

	<i>Time (min)</i>	<i>Recording</i>	<i>Field</i>	<i>Observations</i>
Total time	0:00-0:15	-	-	dark
55:05 min	0:15-10:49	Continuous	Steady	circular periodic structures that evolve in size w.r.t. time (small= \rightarrow large), some larger structures
Notes	10:49-38:28	-	Pulsed	picture goes dark in the first few seconds of pulsed field
	38:28-44:18	Continuous	Steady	circular periodic structures that evolve in size w.r.t. time (small= \rightarrow large), some larger structures/noise, wall shos with finger effect
	44:18-55:05	-	Pulsed	picture goes dark in the first few seconds of pulsed field

Appendix A. *InSPACE* Data Catalog

Cassette ID 141

	<i>Time (min)</i>	<i>Recording</i>	<i>Field</i>	<i>Observations</i>
Total time	0:00-1:14	-	-	dark
55:00 min	1:14-17:49	Continuous	Steady	circular periodic structures (small= \neq large), some larger structures/noise?, wall shot dark but no fingers, structures extremely well defined before pulsed field applied (well focused?)
Notes	17:49-26:12	-	Pulsed	picture goes dark in the first few seconds of pulsed field
	26:12-31:16	Continuous	Steady	circular structures slightly blurred
	31:16-36:48	-	Pulsed	picture goes dark in the first few seconds of pulsed field
	36:48-42:39	Continuous	Steady	circular periodic structures, wall shots w/ fingers visible
	42:39-47:52	-	Pulsed	picture goes dark in the first few seconds of pulsed field
	47:52-53:27	Continuous	Steady	circular periodic structures, some noise
	53:27-54:34	-	Pulsed	picture goes dark in the first few seconds of pulsed field
	54:34-55:00	Continuous	Steady	darker but structures still visible, similar to previous continuous fields

Appendix A. *InSPACE* Data Catalog

Cassette ID 153

	<i>Time (min)</i>	<i>Recording</i>	<i>Field</i>	<i>Observations</i>
Total time	0:00-0:45	-	-	dark
21:20 min	0:45-10:37	Continuous	Steady	cicular periodic structures that progressively get larger, some larger structures/noise, ares of depletion around larger structures
Notes	10:37-15:00	-	Pulsed	picture goes dark in the first few seconds of pulsed field
	15:00-19:05	Continuous	Steady	structures eveolve fromvery fine to coarse, some larger structures w/ areas of depletion
	19:06-21:20	-	Pulsed	picture goes dark in the first few seconds of pulsed field

Appendix A. *InSPACE* Data Catalog

Cassette ID 155

	<i>Time (min)</i>	<i>Recording</i>	<i>Field</i>	<i>Observations</i>
Total time	0:00-1:47	-	-	dark
42:12 min	1:47-14:49	Continuous	Steady	strucutre pattern fine to coarse wrt time, very well defined structures
Notes	14:49-20:00	-	Pulsed	picture goes dark in the first few seconds of pulsed field
	20:00-24:27	Continuous(?)	Steady	circular periodic structures
	24:27-27:50	-	Pulsed	picture goes dark in the first few seconds of pulsed field
	27:50-32:44	Continuous(?)	Steady	visible structures but slightly out of focus
	32:44-37:08	-	Pulsed	picture goes dark in the first few seconds of pulsed field
	37:08-41:41	Continuous	Steady	seems to be wall, left side finger iike structures, right side well defined circular structures
	41:41-42:12	-	Pulsed	picture goes dark in the first few seconds of pulsed field

Appendix A. *InSPACE Data Catalog*

Cassette ID 169

	<i>Time (min)</i>	<i>Recording</i>	<i>Field</i>	<i>Observations</i>
Total time	0:00-0:15	-	-	dark
45:57 min	0:15-14:05	Continuous	Steady	coarsening then aggregation of individual structures, zone of depletion around larger structures
Notes	14:05-18:16	Time-Lapsed	Pulsed	starts to become dark but not fully
	18:16-23:34	Continuous	Steady	continued aggregation, depletion zones, potentially some ejection ?
	23:34-24:48	Continuous	Pulsed	seems out of focus but still very visible, large structure have zones of depletion
	24:48-26:53	Time-Lapsed	Pulsed	continued aggregation into much larger structures
	26:53-32:55	Continuous	Steady	development of more distinctive depletion zones by addition to larger structure or to the smaller surrounding ones
	32:55-37:01	Continuous	Pulsed	ejection and depletion zones, progressively darker but still visible structures in background (snake)
	37:01-43:32	Continuous	Steady	development of several larger snake like structures with periodic structures in between which undergo coarsening
	43:32-45:46	-	Pulsed	picture goes dark in the first few seconds of pulsed field
	45:46-45:51	Continuous	Steady	shows what was going on during pulsed field - similar to previous steady field
	45:51-45:57	-	Pulsed	dark

Appendix A. *InSPACE* Data Catalog

Cassette ID 169 - Steady

	<i>Time (min)</i>	<i>Recording</i>	<i>Field</i>	<i>Observations</i>
Total time	0:00-0:15	-	-	dark
14:00 min	0:15-14:00	Continuous (?)	Steady	coarsening of fine structures, aggregation of individual structures, depletion zones around larger structures

Cassette ID 181

	<i>Time (min)</i>	<i>Recording</i>	<i>Field</i>	<i>Observations</i>
Total time	0:00-42:20	-	-	dark (a few pans from wall to wall but nothing visible)

42:20 min

Notes

Cassette ID 182 - Steady

	<i>Time (min)</i>	<i>Recording</i>	<i>Field</i>	<i>Observations</i>
Total time	0:00-0:25	-	-	dark
14:50 min	0:25-14:50	Continuous (?)	Steady	coarsening of fine structures, aggregation of individual structures

Notes

time runs fast

Appendix A. *InSPACE* Data Catalog

Cassette ID 182

	<i>Time (min)</i>	<i>Recording</i>	<i>Field</i>	<i>Observations</i>
Total time	0:00-0:24	-	-	dark
46:28 min	0:24-14:53	Continuous	Steady	coarsening of fine structures followed by continued aggregation
Notes	14:53-15:15	Continuous	Pulsed	periodic circular structures grow in size with each pulse, some dark spots by end of pulses
	15:15-17:05	Continuous	Steady	darker spots evolve back into individual structures
	17:05-20:00	Time-Lapsed	Pulsed	aggregation of individual structures into larger ones with zones of depletion
	20:00-25:47	Continuous	Steady	some addition to larger structures and some aggregation of residual individual structures, mostly unchanged
	25:47-30:22	Time-Lapsed	Pulsed	ejection from and addition to larger structures
	30:22-34:57	Continuous	Steady	addition to large structures
	34:57-38:40	Continuous	Pulsed	aggregation around larger structures, zones of depletion
	38:40-43:32	Continuous	Steady	less movement in steady field of structures
	43:32-46:28	Time-Lapsed	Pulsed	almost like repulsion of smaller structures as larger structures move (zone of depletion)

Appendix A. *InSPACE Data Catalog*

Cassette ID 183

	<i>Time (min)</i>	<i>Recording</i>	<i>Field</i>	<i>Observations</i>
Total time	0:00-00:33	Continuous	Pulsed	ejection and zones of depletion, initial jump in video
27:02 min	0:33-5:43	Continuous	Steady	creation of larger structures in areas w/ periodic small structures, no addition structures w/ large zones of depletion
Notes	5:43-9:26	Time-Lapsed	Pulsed	ejection and zones of depletion
	9:26-23:32	Continuous	Steady	aggregation
	23:32-26:36	Time-Lapsed	Steady	a few large structures with large zones of depletion
	26:36-27:02	Time-Lapsed	Pulsed	goes dark after first time jump

A.2 InSPACE 1 - RT view

Cassette ID 90

	<i>Time (min)</i>	<i>Recording</i>	<i>Field</i>	<i>Observations</i>
Total time	0:00-55:12	-	-	dark
55:12 min				

Cassette ID 91

	<i>Time (min)</i>	<i>Recording</i>	<i>Field</i>	<i>Observations</i>
Total time	0:00-55:35	-	-	dark
55:35 min				

Cassette ID 101

	<i>Time (min)</i>	<i>Recording</i>	<i>Field</i>	<i>Observations</i>
Total time	0:00-54:03	-	-	dark
54:03 min				

Appendix A. *InSPACE* Data Catalog

Cassette ID 104

	<i>Time (min)</i>	<i>Recording</i>	<i>Field</i>	<i>Observations</i>
Total time	0:00-16:37	-	-	dark
54:03 min	16:37-22:52	-	-	mostly dark but distinguishable bands
Notes	22:52-42:09	-	-	dark
	42:09-46:16	-	-	mostly dark but distinguishable bands
	46:16-54:03	Continuous	Steady	columns coming to end, columns end in spikes, narrower towards the ends

Cassette ID 104B

	<i>Time (min)</i>	<i>Recording</i>	<i>Field</i>	<i>Observations</i>
Total time	0:00-54:57	-	-	dark
54:57 min				

Cassette ID 105

	<i>Time (min)</i>	<i>Recording</i>	<i>Field</i>	<i>Observations</i>
Total time	0:00-15:07	-	-	dark
54:57 min	15:07-34:30	-	-	most dark but some distinguishable bands
Notes	34:30-54:57	-	-	dark

Cassette ID 105/106

	<i>Time (min)</i>	<i>Recording</i>	<i>Field</i>	<i>Observations</i>
Total time	0:00-25:47	-	-	dark
52:55 min	25:47-32:11	-	-	mostly dark but some distinguishable bands, some good shots starting @ 29:43
Notes	32:11-45:48	-	-	dark
	45:48-47:34	-	-	mostly dark some visible structures
	47:34-52:55	-	-	

Appendix A. *InSPACE* Data Catalog

Cassette ID 105B

	<i>Time (min)</i>	<i>Recording</i>	<i>Field</i>	<i>Observations</i>
Total time	0:00-5:55	-	-	dark
49:49 min	5:55-15:00	Time-Lapsed?	Pulsed	fine bands begin to collect to form wider bands
Notes	15:00-30:20	Time-Lapsed	Pulsed	bands continue to collect into medium size, spike like ends of some bands
	30:20-49:49	Time-Lapsed	Pulsed	extremely large bands appear by the end they take over all of viewing screen

Cassette ID 106

	<i>Time (min)</i>	<i>Recording</i>	<i>Field</i>	<i>Observations</i>
Total time	0:00-55:04	-	-	dark, possibly something towards the end
54:04 min				

Cassette ID 106/107

	<i>Time (min)</i>	<i>Recording</i>	<i>Field</i>	<i>Observations</i>
Total time	0:00-22:58	-	-	dark
54:04 min	22:58-25:55	Time-Lapsed	pulsed	some visible bands, mostly dark
Notes	25:55-54:04			dark

Cassette ID 107

	<i>Time (min)</i>	<i>Recording</i>	<i>Field</i>	<i>Observations</i>
Total time	0:00-14:06	-	-	dark
55:02 min	14:06-17:00	Continuous	-	very fine bands almost dark
Notes	17:00-55:02			dark, possibly some bands at the end but too dark to discern

Appendix A. *InSPACE* Data Catalog

Cassette ID 119

	<i>Time (min)</i>	<i>Recording</i>	<i>Field</i>	<i>Observations</i>
Total time	0:00-52:34	-	-	dark
55:02 min	52:34-54:42	-	-	very dark but some visible bands
Notes	54:42-55:02	-	-	dark

Cassette ID 139

	<i>Time (min)</i>	<i>Recording</i>	<i>Field</i>	<i>Observations</i>
Total time	0:00-42:45	-	-	dark
55:05 min	42:45-48:05	-	-	very dark but some visible bands
Notes	48:05-53:24	-	-	dark
	53:24-55:05	-	Pulsed	very dark but some structures

Cassette ID 141

	<i>Time (min)</i>	<i>Recording</i>	<i>Field</i>	<i>Observations</i>
Total time	0:00-19:42	-	-	dark
55:05 min	19:42-26:30	-	-	mostly dark - some bands visible
Notes	26:30-31:30	-	-	dark
	31:30-55:05	-	-	some structures visible

Cassette ID 143

	<i>Time (min)</i>	<i>Recording</i>	<i>Field</i>	<i>Observations</i>
Total time	0:00-55:13	-	-	dark
55:13 min				

Cassette ID 153

	<i>Time (min)</i>	<i>Recording</i>	<i>Field</i>	<i>Observations</i>
Total time	0:00-55:02	-	-	dark
55:02 min				

Cassette ID 153B

	<i>Time (min)</i>	<i>Recording</i>	<i>Field</i>	<i>Observations</i>
Total time	0:00-23:35	-	-	dark
21:35 min				

Appendix A. *InSPACE* Data Catalog

Cassette ID 161

	<i>Time (min)</i>	<i>Recording</i>	<i>Field</i>	<i>Observations</i>
Total time	0:00-23:23	-	-	dark
52:42 min	23:23-31:42	Continuous	Steady	some darkness but distinguishable bands
Notes	31:42-33:39	Time-Lapsed	Pulsed	some dark, mostly larger bands w/ smaller ones in between
	33:39-39:26	Continuous	Steady	thinning out of of larger bands into smaller ones
	39:26-41:25	Continuous	Pulsed	becomes darker w/ bands coming together
	41:25-43:16	Time-Lapsed	Pulsed	continued
	43:16-48:44	Continuous	Steady	thinning to smaller bands but some large bands still remain
	48:44-50:33	Continuous	Pulsed	aggregation into larger bands
	50:33-52:22	Time-Lapsed	Pulsed	continued
	52:22-52:42	Time-Lapsed	Steady	relatively dark

Cassette ID 178

	<i>Time (min)</i>	<i>Recording</i>	<i>Field</i>	<i>Observations</i>
Total time	0:00-49:04			
49:04 min		-	-	dark

Appendix A. *InSPACE* Data Catalog

Cassette ID 183

	<i>Time (min)</i>	<i>Recording</i>	<i>Field</i>	<i>Observations</i>
Total time	0:00-19:51	-	-	dark
49:19 min	19:51-20:29	Time-Lapsed	Steady	most dark but start of structures
Notes	20:29-22:40	Time-Lapsed	Steady	wide bands with wide gaps (zones of depletion?)
	22:40-29:06	Continuous	Steady	a few large bands with smaller ones interspersed
	29:06-31:45	Time-Lapsed	Steady	progressively darker (pulsed?)
	31:45-39:19	Continuous	Steady	top dark, bottom shows individual small bands in gaps of big ones
	39:19-40:37	Time-Lapsed	Steady	same
	40:37-45:47	Continuous		same
	45:47-48:53	Time-Lapsed		small bands on top and bottom of picture moving in the gaps
	48:53-49:19	-	-	dark